In situ electrochemically synthesized Pt-MoO$_{3-x}$ nanostructure catalysts for efficient hydrogen evolution reaction

Daewon Lee [a], Youngmin Kim [a], Hyun Woo Kim [b], Min Choi [b,c], Noejung Park [d], Hyunju Chang [b], Youngkook Kwon [a,e], Jong Hyeok Park [f], Hyung Ju Kim [a,e,*]

[a] Carbon Resources Institute, Korea Research Institute of Chemical Technology (KRICT), 141 Gajeong-ro, Yuseong-gu, Daejeon 34114, South Korea
[b] Center for Molecular Modeling and Simulation, Korea Research Institute of Chemical Technology (KRICT), 141 Gajeong-ro, Yuseong-gu, Daejeon 34114, South Korea
[c] Department of Chemistry, Ulsan National Institute of Science and Technology (UNIST), 50, UNIST-gil, Banyeon-ri, Eonyang-eup, Ulju-gun, Ulsan 44919, South Korea
[d] Department of Physics, Ulsan National Institute of Science and Technology (UNIST), 50, UNIST-gil, Banyeon-ri, Eonyang-eup, Ulju-gun, Ulsan 44919, South Korea
[e] Advanced Materials and Chemical Engineering, University of Science and Technology (UST), 113 Gwahangno, Yuseong-gu, Daejeon 34113, South Korea
[f] Department of Chemical and Biomolecular Engineering, Yonsei University, 50 Yonsei-ro, Seodaemun-gu, Seoul 03722, South Korea

ARTICLE INFO

ABSTRACT

Designing and preparing highly active and stable nanostructured Pt-based catalysts with ultralow Pt loading are still challenging for electrochemical applications such as water electrolysis and fuel cells. Here we report for the first time an *in situ* electrochemical process to synthesize Pt-MoO$_{3-x}$ nanoflakes (NFs) overgrown on commercial bulk MoS$_2$ by employing a facile and simple electrochemical method without using any expensive precious metal salts. The overgrowth of Pt-MoO$_{3-x}$ NFs on the bulk MoS$_2$ surface is conducted by applying electrical energy to the bulk MoS$_2$ and using Pt counter electrode dissolution in an acidic solution. In spite of their 10 times lower Pt loadings compared to commercial Pt black (Alfa Aesar), the synthesized Pt-MoO$_{3-x}$ NFs demonstrate excellent catalytic performance with a Pt mass activity of 2.83 A/mg$_{Pt}$ at the overpotential of 100 mV for electrochemical hydrogen evolution reaction (HER), an approximately 4 times higher value than the value of 0.76 A/mg$_{Pt}$ at the overpotential of 100 mV for commercial Pt black. We hypothesize that the outstanding HER characteristics of Pt-MoO$_{3-x}$ NFs are related to the existence and increase of Pt-MoO$_3$ interfacial sites and oxygen vacancy sites such as Mo^{5+} in the Pt-MoO$_{3-x}$ NF structures. In addition, our density functional theory (DFT) calculations demonstrate that Pt and O sites at Pt and MoO$_3$ interfaces and O sites at defective MoO$_{3-x}$ in the Pt-MoO$_{3-x}$ NFs contribute to accelerate the HER.

© 2019 Elsevier Inc. All rights reserved.

1. Introduction

Molybdenum (Mo) based materials such as molybdenum disulfide (MoS$_2$) and molybdenum oxide (MoO$_3$), with layered crystalline structures, are very attractive materials for catalysis, transistors, and capacitors due to their unique physical and chemical features [1–16]. MoS$_2$ has a common polytype 2H phase crystal structure that is composed of weakly interacting layers held together by van der Waals forces [10,17,18]. Recently, many researchers have become interested in the use of MoS$_2$ for electrochemical storage, photodetectors, electrocatalysis, and transistors [4,10,19–28]. Also, since the first report suggesting that undercoordinated S atoms at the edges of MoS$_2$ can be active centers for the HER, MoS$_2$ has been extensively studied as a promising electrocatalyst for the hydrogen evolution reaction (HER) [29]. It has been well documented that the electrocatalytic HER performance is

dependent on the number of catalytically active edge sites of MoS$_2$ [1,19,30–33]. MoO$_3$ is also an interesting material, having a layered structure with stacked bilayer sheets of MoO$_6$ octahedra held together by van der Waals interactions [6,8]. This MoO$_3$ structure has been intensively studied as a material for pseudocapacitors and lithium ion batteries because of its ability for insertion/removal of small ions such as Li$^+$ [2,3,6,9,34,35]. However, as a HER electrocatalyst, the intrinsic MoO$_3$ material has poor electrocatalytic performance due to a lack of active sites like edge sites of MoS$_2$ [36]. It has recently been reported that creating oxygen vacancies in the MoO$_3$ lattice structure can lead to enhanced electrochemical performance for pseudocapacitive charge storage and electrocatalytic HER [9,36,37]. In addition, oxygen vacancies close to Mo^{5+} in the oxygen deficient MoO$_{3-x}$ structure are found to be active sites for the electrocatalytic HER [36,37]. However, despite numerous efforts to develop Mo-based HER catalysts such as MoS$_2$ and MoO$_{3-x}$, the Mo-based catalysts themselves are still not active and/or stable compared with conventional Pt-based electrocatalysts for the HER [37–41].

A good strategy for improving the HER performance of Mo-based catalysts is to incorporate very small amounts of active noble metals such as platinum (Pt). In this regard, for novel active HER electrocatalysts, there exist several reports on the synthesis of MoS_2 materials decorated with Pt, palladium (Pd), and gold (Au) via chemical synthesis, assembling, and solvothermal methods [40–44]. Synergistic effects between precious metals and MoS_2 bring about the enhanced HER characteristics. Besides MoS_2, some groups have reported on Pt-MoO_x hybrids as catalysts for electro-oxidation reactions; these materials were prepared by electrochemical co-deposition and precipitation-reduction methods [45,46]. However, the aforementioned synthetic strategies are somewhat complicated and indispensably exploit high-priced precious metal precursors (e.g. H_2PtCl_6, K_2PtCl_6, $Pd(C_5H_7O_2)_2$, and $HAuCl_4$) as metal source to fabricate electrocatalysts combined with metal and Mo-based materials. Taking into account this issue, some research groups have recently reported on the electrochemical deposition of Pt on a variety of substrate materials through anodic dissolution of Pt counter electrodes and subsequent deposition of Pt on working electrode substrates, so as to create novel HER electrocatalysts with low Pt loading [39,47–53]. It should be noted that the utilization of Pt counter electrode as a solid metal source can pave the facile and efficient route to prepare high performance electrocatalysts; this is because it does not require both sophisticated synthesis methods and expensive noble metal precursors. Nevertheless, there have been only rare reports on electrochemical synthesis by Pt counter dissolution, especially focusing on control of the nanostructure and creation of novel catalytic active sites for HER. In this light, it is highly desirable to develop a facile, nontoxic, and low-cost synthetic method using dissolution and re-deposition technique of a Pt counter electrode and/or other solid metals, in order to achieve well-defined nanostructure materials and gain fundamental mechanistic insight into the synthesized materials to promote electrocatalytic HER.

Herein, we present the first report of in situ electrochemical synthesis of Pt-$MoO_{3−x}$ nanoflakes grown on a commercial bulk MoS_2 material by applying electrical energy to the bulk MoS_2 and utilizing Pt counter electrode corrosion in an acidic solution. These novel Pt-$MoO_{3−x}$ nanostructures comprising nanoflakes (NFs) and/or nanoparticles (NPs) on a bulk MoS_2 substrate are controlled by using a very easy, simple, and scalable electrochemical method. The Pt-$MoO_{3−x}$ NFs grown on bulk MoS_2 significantly improve the electrochemical HER performances and the rate of HER reaction over this catalyst, and these enhanced HER abilities are 3.7 times higher Pt mass activity than conventional Pt black electrocatalyst. The enhanced HER features of Pt-$MoO_{3−x}$ NFs are associated with the formation of Pt-MoO_3 interfacial sites and the existence of more oxygen vacancies close to Mo^{5+} as the HER active sites in the as-synthesized Pt-$MoO_{3−x}$ NF structures. Density functional theory (DFT) calculations also support that HER over the synthesized Pt-$MoO_{3−x}$ nanostructures can be promoted by Pt and O sites near the interfaces of Pt-MoO_3 surfaces, and O atoms at the defects of $MoO_{3−x}$ surfaces. In addition, this facile and cost-effective synthetic technology has the advantage of creating new HER active sites without use of any expensive precious metal salts, and it can be easily scaled up for large-scale synthesis of outstanding HER electrocatalysts because it does not require any sophisticated synthetic methods or expensive noble metal precursors.

2. Experimental

2.1. In situ electrochemical synthesis

In situ electrochemical synthesis of nanostructured Pt-$MoO_{3−x}$ grown on bulk MoS_2 catalysts was conducted using a customized glass-type cell system. To fabricate the working electrode, an ink solution was prepared by dispersing commercial bulk MoS_2 (<2 μm, 99%, Sigma-Aldrich) in a solution comprising distilled water, 2-propanol (99.5%, Samchun Pure Chemical), and 5 wt% Nafion® solution (D521, DuPont) via sonication for 1 h. The working electrode was made by means of spray coating on carbon paper (TGP-H-090, Toray) of the ink solution with dispersed MoS_2. The MoS_2-coated carbon paper electrode was dried in a convection oven for 1 h at a temperature of 373 K; finally, a thin MoS_2 layer was created on the carbon paper with a loaded amount of 0.4 mg/cm². The in situ electrochemical synthesis was performed at room temperature in a 0.5 M H_2SO_4 solution (Samchun Pure Chemical) using a potentiostat (ZIVE MP2A, WonATech). An Ag/AgCl/KCl (1 M) electrode and Pt wire served as reference and counter electrodes, respectively. For the overgrowth of nanostructured Pt-$MoO_{3−x}$ on bulk MoS_2, the chronoamperometry method was used to apply a potential of −0.31 or −0.46 V (vs. SHE) with proper time. The reaction conditions including the total amount of electrical energy applied to the bulk MoS_2 coated electrodes are summarized in Table S1.

2.2. Physicochemical characterizations

Scanning electron microscopy (SEM) images were obtained from a field-emission SEM (SU8230, Hitachi). A field-emission transmission electron microscopy (TEM) (Tecnai G^2 F30 S-TWIN, FEI) was used to obtain TEM images under an acceleration voltage of 300 kV. We exploited a double Cs-corrected TEM (Titan Cubed G^2 60–300, FEI) at an acceleration voltage of 300 kV to acquire high-angle annular dark-field scanning TEM (HAADF-STEM) images and corresponding energy dispersive X-ray spectroscopy (EDS) elemental mapping results. The existence of Pt and Mo ionic species in the electrolyte solution and the Pt loading amount of the synthesized sample were determined by inductively coupled plasma optical emission spectrometry (ICP-OES) (iCAP 6300 Duo view, Thermo Scientific). EDS elemental analysis was performed using an energy dispersive X-ray spectrometer (QUANTAX 200, Bruker). X-ray diffraction (XRD) patterns were recorded using a multipurpose X-ray diffractometer with a Cu Kα Source (Ultima IV, Rigaku). Raman spectra were obtained from a high-resolution Raman/photoluminescence spectrophotometer with laser excitation at 514 nm (LabRAM HR Evolution, Horiba). X-ray photoelectron spectroscopy (XPS) spectra were measured by a multipurpose X-ray photoelectron spectrometer with an Al Kα Source (Sigma Probe, Thermo Scientific). Note that the binding energies of the XPS spectra were corrected using the C 1s line (284.5 eV) as a reference. Synchrotron-based X-ray absorption spectroscopy (XAS) analysis at both the L_3-edge of Pt (11,564 eV) and K-edge of Mo (19999.5 eV), comprising X-ray absorption near the edge structure (XANES) and extended X-ray absorption fine structure (EXAFS), was conducted on the 7D beamline of the Pohang Accelerator Laboratory using a Si (1 1 1) double crystal monochromator (PLS-II, 3.0 GeV, Republic of Korea).

2.3. Electrochemical performance measurement

After the in situ electrochemical synthesis, the Pt-$MoO_{3−x}$ nanostructure samples overgrown on bulk MoS_2 coated carbon paper as the working electrodes were tested to measure the electrochemical HER performance in an electrochemical cell having a three-electrode system. For performance comparison, bulk MoS_2 and commercial Pt black (high surface area, Alfa Aesar), spray-coated on carbon papers with the same loaded amount of 0.4 mg/cm², were also examined under the same conditions. The electrochemical analysis of the HER was performed under ambient conditions in a 0.5 M H_2SO_4 aqueous solution with a potentiostat. Counter and reference electrodes were a glassy carbon rod and

an Ag/AgCl/KCl (1 M) electrode, respectively. The polarization curve was recorded from 0.29 V to −0.81 V (*vs.* SHE) at a scan rate of 5 mV/s *via* the linear sweep voltammetry method, and then the measured polarization curve was *iR*-compensated. To obtain a Nyquist plot, electrochemical impedance spectroscopy was performed at −0.21 V (*vs.* SHE) over a frequency range from 100 kHz to 0.1 Hz with an amplitude of 5 mV. The chronopotentiometry test was conducted at a constant current of −10 mA/cm^2 for 100 h. To calculate the H$_2$ Faradaic efficiency, a gas chromatograph (μTCD detector, DS Science) equipped with a Molecular Sieve 5A column (Restek) was used to analyze the amount of H$_2$ gas produced during the electrochemical HER. For electrochemically active surface area (ECSA) analysis, cyclic voltammetry (CV) in a 0.5 M H$_2$SO$_4$ electrolyte solution was performed at different scan rates of 10, 20, 30, 40, and 50 mV/s within a potential region of 0.1–0.2 V (*vs.* SHE) in order to determine the electrochemical double layer capacitance (C$_{dl}$). We assumed that only non-Faradaic processes take place at the electrode-solution interface in this potential range; in detail, all the measured current density values were assumed to stem from double layer charging in the selected potential region. From the recorded CV curves, C$_{dl}$ was calculated according to Eq. (1),

$$\frac{\Delta J_{0.15V}}{2} = \nu C_{dl} \qquad (1)$$

where $\Delta J_{0.15\,V}$ is the difference between the cathodic and anodic current density at 0.15 V (*vs.* SHE) (*i.e.* the center of the potential range) and ν is the scan rate. In other words, C$_{dl}$ is the slope of the fitted straight line plotting $\Delta J_{0.15\,V}/2$ *vs. ν*.

2.4. Computational details

We performed all first-principle calculations with the Vienna *Ab initio* Simulation Package (VASP) [54,55]. We adopted optB88-vdW functional [56,57] following a previous study on defective MoO$_3$ surfaces [9]. The energy cutoff of a plane wave basis set was set to 520 eV and atomic pseudopotentials were described with the projector augmented wave (PAW) method. MoO$_3$(0 1 0) and Pt (1 1 1) surfaces were prepared in 3 × 3 super-cells, which consist of four and five layers, respectively. For these surfaces, 3 × 3 × 1 Monkhorst-Pack **k**-point grids were used to sample the Brillouin zone. Mixed surfaces of MoO$_3$ and Pt were generated by overlaying the MoO$_3$(0 1 0) surface with a large rectangular unit cell of a Pt (1 1 1) surface and then removing Pt atoms located too close to the Mo or O atoms on MoO$_3$(0 1 0) surface. The size of this unit cell was 11.265 × 24.1 × 36.0 Å^3 as it was optimized along the edge that contains both MoO$_3$ and Pt domains. This mixed surface has 36 Mo, 120 O, and 82 Pt atoms, and a 3 × 1 × 1 Monkhorst-Pack **k**-point mesh used as the unit cell became larger than the MoO$_3$ or Pt surfaces. Hydrogen adsorption energies (ΔE_H) were estimated according to Eq. (2),

$$\Delta E_H = E_{surf+H} - E_{surf} - \frac{1}{2}E_{H2} \qquad (2)$$

where E_{surf+H}, E_{surf}, and E_{H2} are the energy of a surface with a hydrogen atom, the surface, and a hydrogen molecule, respectively. The free energy for hydrogen adsorption (ΔG_H) was calculated by adjusting contributions from the zero-point motion and the entropic effect, as was done in the Ref. [58].

3. Results and discussion

3.1. In situ electrochemical synthesis

The *in situ* electrochemical synthesis process of the nanostructured Pt-MoO$_{3-x}$ grown on bulk MoS$_2$ is graphically illustrated in

Fig. 1. We chose a commercial bulk MoS$_2$ as the substrate material for the *in situ* electrochemical nanostructuring process. The bulk MoS$_2$ was deposited on carbon paper electrodes using a spraying method. Interestingly, the formation of the nanostructured Pt-MoO$_{3-x}$ on the bulk MoS$_2$ surface was observed when sufficient electrical energy was applied to bulk MoS$_2$ coated carbon paper electrode in a 0.5 M H$_2$SO$_4$ aqueous solution under ambient conditions. In detail, the Pt-MoO$_{3-x}$ NPs initially emerge from the surface of bulk MoS$_2$ (Pt-MoO$_{3-x}$ NPs ¦ MoS$_2$), and then gradually cover most of the MoS$_2$ surface (Pt-MoO$_{3-x}$ NPs | MoS$_2$). The accumulation of Pt-MoO$_{3-x}$ NPs on bulk MoS$_2$ leads to interaction between the NPs and thereby growth of the Pt-MoO$_{3-x}$ NFs (Pt-MoO$_{3-x}$ NFPs | MoS$_2$), which have randomly oriented Pt-MoO$_{3-x}$ NPs as building blocks. Consequently, Pt-MoO$_{3-x}$ NFs fully cover the entire surface of bulk MoS$_2$ *via* the complete morphological transformation from NPs into NFs (Pt-MoO$_{3-x}$ NFs | MoS$_2$). It is worthwhile to note that applying more electrical energy to the bulk MoS$_2$ coated electrode is required to progress to the subsequent stages of this *in situ* electrochemical synthesis. In this study, the chronoamperometry method was used to modulate the amount of electrical energy applied to bulk MoS$_2$; this involved varying the electrical potentials (*i.e.* cathodic potentials) and times (see Fig. S1 and Table S1).

3.2. Morphological analysis of Pt-MoO$_{3-x}$ nanostructures

As presented in Figs. 2 and S6, SEM and TEM analyses reveal sequential growth of the nanostructured Pt-MoO$_{3-x}$ on the bulk MoS$_2$ surface according to the amount of electrical energy applied to the bulk MoS$_2$ coated electrode. Commercial bulk MoS$_2$ was used as the starting material. This material exhibits a two dimensional (2D) layered structure with dimensions of less than 2 μm (Bulk MoS$_2$ in Figs. 2 and S2), consistent with the representative structure for transition-metal dichalcogenides. The 2D bulk MoS$_2$ material can be a good substrate material for growing and establishing nanostructures on its basal plane sites, which comprise the majority of bulk MoS$_2$ and have large surface area. First, applying electrical energy of ~0.00059 kWh (electrical potential: −0.31 V *vs.* standard hydrogen electrode (SHE), time: 60 h) to the bulk MoS$_2$ generates crystalline Pt-MoO$_{3-x}$ NPs, with a wide size distribution of 4–11 nm, over the surface of the bulk MoS$_2$ (Pt-MoO$_{3-x}$ NPs ¦ MoS$_2$ in Figs. 2 and S3). An applied electrical energy of ~0.0021 kWh (electrical potential: −0.31 V *vs.* SHE, time: 72 h) is required to cover most of the MoS$_2$ surface with Pt-MoO$_{3-x}$ NPs (Pt-MoO$_{3-x}$ NPs | MoS$_2$ in Figs. 2 and S4). When the total applied electrical energy reaches ~0.0031 kWh (electrical potential: −0.31 V *vs.* SHE, time: 96 h), a morphological transformation from spherical-like NPs to NF structures (*i.e.* the growth of Pt-MoO$_{3-x}$ NFs) occurs via the interaction between preformed Pt-MoO$_{3-x}$ NPs on bulk MoS$_2$, lowering their surface energy (Pt-MoO$_{3-x}$ NFPs | MoS$_2$ in Figs. 2 and S5). Finally, by applying the electrical energy of ~0.0035 kWh (electrical potential: −0.46 V *vs.* SHE, time: 42 h), the overall surface of bulk MoS$_2$ is fully covered with Pt-MoO$_{3-x}$ NFs. The Pt-MoO$_{3-x}$ NFs grown on bulk MoS$_2$ have ranges of 100–200 nm in length and 40–80 nm in width, and are combined with randomly oriented crystalline Pt-MoO$_{3-x}$ NPs (Pt-MoO$_{3-x}$ NFs | MoS$_2$ in Figs. 2 and 3).

Ionic Pt and Mo precursors are required for the *in situ* electrochemical growth of the nanostructured Pt-MoO$_{3-x}$ on bulk MoS$_2$ surface. It has been reported that Pt deposition on various working electrode substrates was observed due to the corrosion of Pt counter electrodes [39,47–52]. The Pt deposition proceeds according to oxidation-dissolution-deposition processes of Pt [51,59]. The Pt surface atoms adsorb oxygenated species from water in anodic potential ranges to create oxidized Pt-O. The oxidized Pt-O is
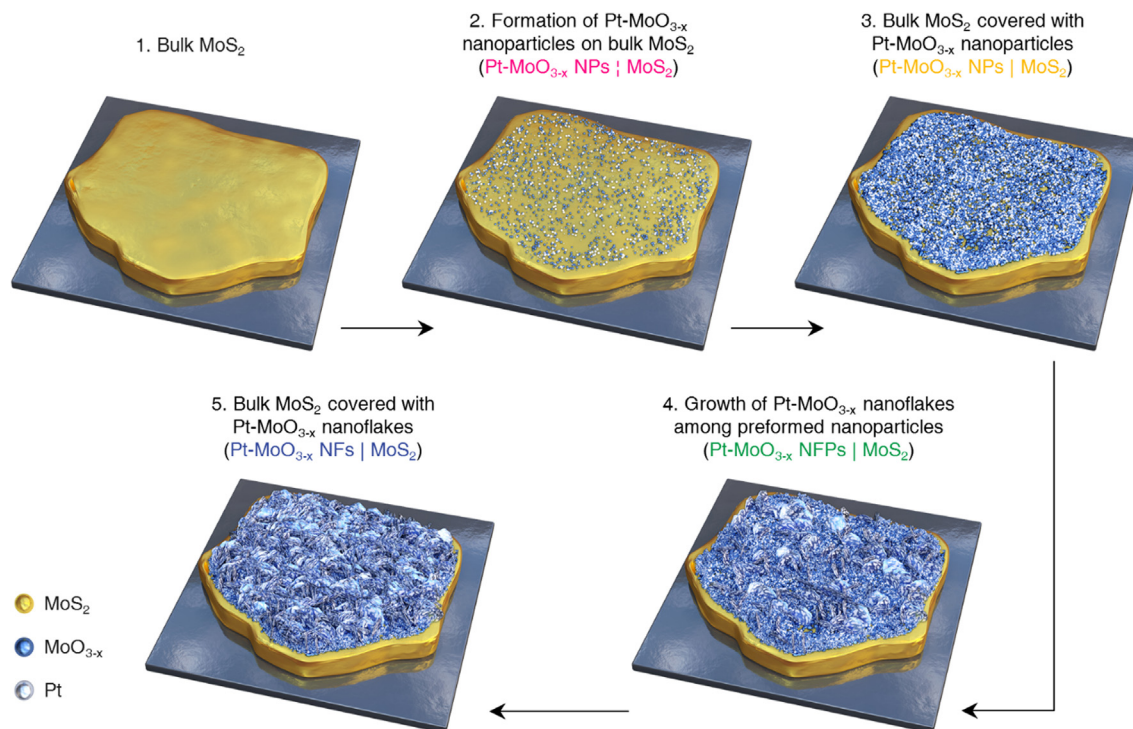
Fig. 1. Schematic illustration of formation of nanostructured Pt-MoO$_{3-x}$ grown on bulk MoS$_2$ surface *via in situ* electrochemical synthesis process.

unstable and dissolves into Pt ions. Depending on Pt ion concentrations, the dissolved Pt ions can re-deposit on the working electrode substrates under cathodic potentials. In addition, etching of MoS$_2$ sub-monolayers by immersing the MoS$_2$ in aqueous media (*i.e.* water) was reported recently [60]. The dissolved MoS$_2$ surface layers can provide ionic Mo sources for electrochemical nanostructure growth on the MoS$_2$ surface. In other words, along with a Pt counter electrode, we used MoS$_2$ as another solid phase starting material for the electrochemical synthesis of Pt-MoO$_{3-x}$ nanostructures on bulk MoS$_2$. After immersion of the bulk MoS$_2$ coated carbon paper electrode in a 0.5 M H$_2$SO$_4$ electrolyte, dissolved Mo species was detected by ICP-OES (Table S2). Also, we confirmed the existence of Pt (0.27 ppm) and Mo (1.43 ppm) dissolved in the electrolyte solution after *in situ* electrochemical synthesis using ICP-OES (Table S2). In addition to the existence of such ionic Pt and Mo species, with oxygen sources (*e.g.* water) in the electrolyte solution, the application of cathodic potential to the bulk MoS$_2$ coated carbon paper electrode contributes to the growth of the Pt-MoO$_{3-x}$ nanostructure. It has been reported that metal and/or metal oxide nanoparticles can be synthesized by cathodic corrosion of bulk metal surfaces in an aqueous phase and subsequent nanoparticle growth of dissolved metal ions produced by bulk metal surface corrosion [61–63]. In particular, after the formation of metal nanoparticles under the negative potential region, metal oxide nanoparticles such as H$_2$WO$_4$ and BiVO$_4$ are produced by the following oxidation process by oxygen sources present in aqueous electrolytes, such as H$_2$O, O$_2$, or OH$^-$ [63]. Furthermore, some studies have reported the preparation of electrodeposited Mo oxide thin films and wires by applying negative potential in electrolyte solutions with dissolved Mo ionic species [64–66]. We also found that the formation of nanostructured Pt-MoO$_{3-x}$ was not observed in the absence of applied negative potential (Fig. S7). It should be noted that the rapidly increased current density in the *I-t* profiles recorded *via* the chronoamperometry method might be evidence of the overgrowth of nanostructured Pt-MoO$_{3-x}$ (Fig. S1). However, future studies should include in-depth analysis

of the detailed overgrowth mechanism of the Pt-MoO$_{3-x}$ nanostructure.

3.3. Physicochemical analyses of Pt-MoO$_{3-x}$ nanostructures

We performed HAADF-STEM analysis coupled with corresponding EDS to measure the elemental composition of the overgrown NFs on bulk MoS$_2$. As shown in Fig. 3, the EDS elemental mapping results of Pt and/or Mo, obtained from the overgrown Pt-MoO$_{3-x}$ NF show uniform distribution of Pt and Mo within the NF structure, proving that the overgrown NFs comprise both Pt and Mo species. From the XRD and Raman spectra results (Fig. S8), no obvious characteristic peaks associated with the existence of the synthesized nanostructures are observed, indicating that a more detailed surface analysis is required. For further detailed surface analysis, the surface chemical and electronic states of the Pt-MoO$_{3-x}$ nanostructures grown on bulk MoS$_2$ were identified by XPS analysis (Figs. 4a and 5a and Table 1 and 3). The XPS binding energies were corrected by referencing the C 1s line at 284.5 eV. To examine and understand the local atomic structure of the electrochemically grown Pt-MoO$_{3-x}$ nanostructures on a more detailed level, we also carried out XAS analysis that comprises the normalized XANES and the corresponding Fourier-transformed EXAFS (FT-EXAFS) (Fig. 4b, c, 5b, c, S9, and S10, and Table 2). The XPS and XAS results for Pt and Mo-related species (*i.e.* Mo, O, and S) are provided separately in Figs. 4 and 5, respectively, so that we can clearly elucidate the structural and electronic features of the overgrown Pt-MoO$_{3-x}$ nanostructures.

In Fig. 4, we display both the high-resolution Pt *4f* XPS spectra of Pt-MoO$_{3-x}$ NFs | MoS$_2$, Pt-MoO$_{3-x}$ NFPs | MoS$_2$, Pt-MoO$_{3-x}$ NPs ¦ MoS$_2$ and a commercial Pt black, and the normalized XANES with the corresponding FT-EXAFS spectra at the Pt *L$_3$*-edge for Pt-MoO$_{3-x}$ NFs | MoS$_2$ and Pt black samples. As presented in the Pt *4f* XPS spectra in Fig. 4a, the individual Pt *4f$_{7/2}$* and Pt *4f$_{5/2}$* doublets are deconvoluted into two oxidation states of metallic Pt^0 (71.0–
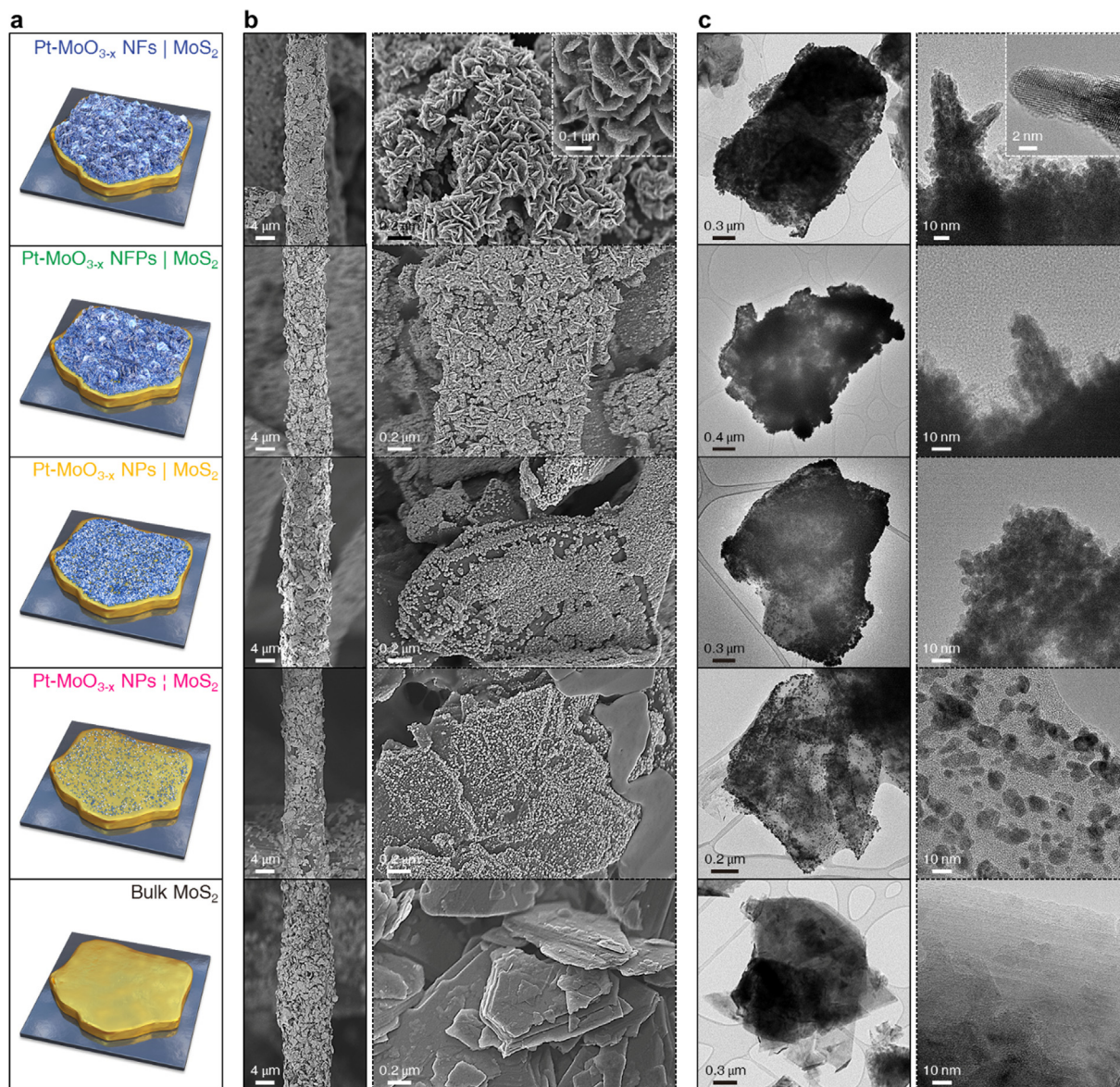
Fig. 2. Electron microscopy analysis elucidating growth of Pt-MoO$_{3-x}$ nanostructures on bulk MoS$_2$ surface *via in situ* electrochemical synthesis process. (a) Schematic illustration depicting each step of *in situ* electrochemical synthesis. (b, c) SEM (b) and TEM (c) images for Pt-MoO$_{3-x}$ NFs | MoS$_2$, Pt-MoO$_{3-x}$ NFPs | MoS$_2$, Pt-MoO$_{3-x}$ NPs | MoS$_2$, Pt-MoO$_{3-x}$ NPs ¦ MoS$_2$, and bulk MoS$_2$ loaded on carbon paper electrode, which are in one-one correspondence with illustrations in (a). Note that the left-hand SEM images in (b) are showing the configuration of coated materials on the carbon fiber constituting the carbon paper electrode. Inset SEM (b) and TEM (c) images obtained from Pt-MoO$_{3-x}$ NFs | MoS$_2$ display detailed NF morphology.

71.7 and 74.4–75.0 eV) and oxidized Pt^{2+} (71.7–72.7 and 75.0–76.0 eV). In terms of the synthesized Pt-MoO$_{3-x}$ nanostructures on bulk MoS$_2$, the binding energies of assigned Pt^0 and Pt^{2+} peaks are shifted to lower values as the Pt-MoO$_{3-x}$ NPs are electrochemically transformed into Pt-MoO$_{3-x}$ NFs: 71.7 → 71.0 and 75.0 → 74.4 eV for Pt^0 and 72.7 → 71.7 and 76.0 → 75.0 eV for Pt^{2+}. These shifts of the Pt *4f* electron binding energies observed in the Pt core level are attributed to the probable filling of the Pt valence band with donated electrons [67,68]. Thus, as *in situ* electrochemical synthesis proceeds, we believe that Pt species on the overgrown Pt-MoO$_{3-x}$ nanostructures accept more electrons from other adjacent heterogeneous constituents (*e.g.* Mo and/or O species) of the synthesized nanostructures. Compared to the commercial Pt black, the binding energies of the Pt species from the fully converted Pt-MoO$_{3-x}$ NFs | MoS$_2$ (71.0 and 74.4 for Pt^0 and 71.7 and 75.0 for Pt^{2+}) are lower than those of Pt black (71.3 and 74.6 eV for Pt^0 and 71.9 and 75.2 eV for Pt^{2+}). Regarding the Pt oxidation state, it

is noteworthy that the Pt^0 state ($\approx$56.0%) was predominant in the Pt-MoO$_{3-x}$ NFs | MoS$_2$, contrary to the dominant Pt^{2+} state ($\approx$71.3%) in the Pt black (Table 1).

As shown in Fig. 4b, the normalized Pt L_3-edge XANES spectra recorded from Pt-MoO$_{3-x}$ NFs | MoS$_2$ and Pt black do not show any noticeable difference in terms of their position and shape. The complementary FT-EXAFS spectra for both Pt-MoO$_{3-x}$ NFs | MoS$_2$ and Pt black possess analogous forms (Fig. 4c). Moreover, there is no perceptible advent of novel spectral peaks, which implies newly formed metal-metal bonds in the FT-EXAFS spectrum of Pt-MoO$_{3-x}$ NFs | MoS$_2$: this is attributed to the fact that Pt-Pt and Mo-Mo peaks are similar in terms of bond distance [69] Given the distinct peak shapes of the Pt-Pt scattering peak at around 2.66 Å, Pt L_3-edge EXAFS curve fitting can reveal another metal-metal bond contribution in Pt-MoO$_{3-x}$ NFs | MoS$_2$, except for the Pt-Pt bond. Along with the fitted curves, the k^3-weighted raw EXAFS function and the real and imaginary parts of respective k^3-
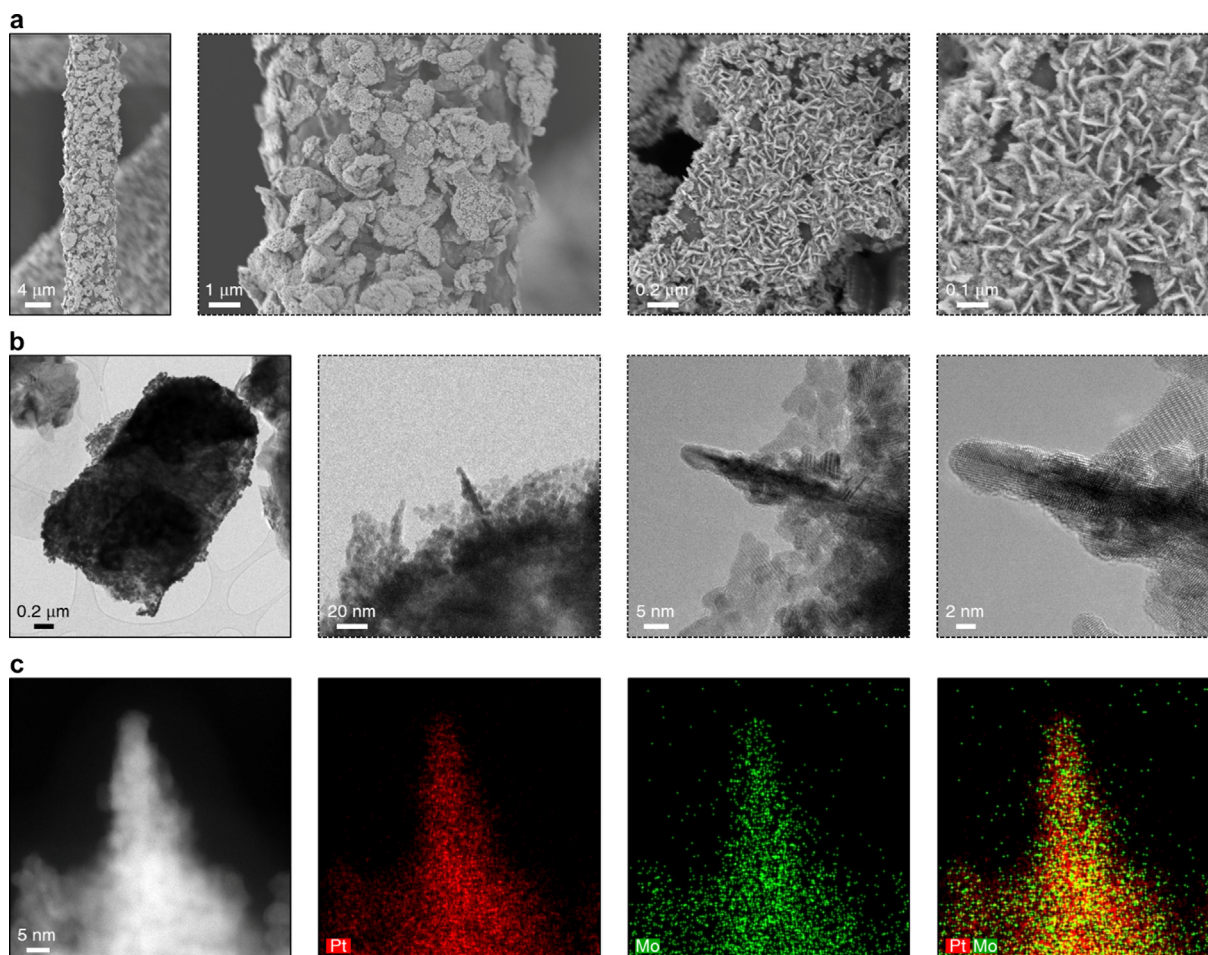
Fig. 3. Electron microscopy analysis results clearly representing the morphology and elemental constituents of the synthesized Pt-MoO$_{3-x}$ NFs on bulk MoS$_2$. (a, b) SEM (a) and TEM (b) images for Pt-MoO$_{3-x}$ NFs | MoS$_2$ loaded on carbon paper electrode. (c) HAADF-STEM image and corresponding EDS elemental mapping of Pt, Mo, and the composite of Pt and Mo obtained from Pt-MoO$_{3-x}$ NFs | MoS$_2$.

weighted FT-EXAFS spectra for both samples are illustrated in Figs. S9 and S10; the derived average coordination number and bond distance values for each shell are tabulated in Table 2. The fitting results corroborate that the existence of Pt-Mo scattering at ~2.70 Å in Pt-MoO$_{3-x}$ NFs | MoS$_2$ is responsible for the aforementioned deviated FT-EXAFS Pt-Pt peak shape compared to that of Pt black [69]. In addition to the Pt-Mo contribution, the Pt-Pt coordination number of ~8.96 and the Pt-Pt bond distance of ~2.74 Å from Pt-MoO$_{3-x}$ NFs | MoS$_2$, with respect to those in Pt black (~8.57 and ~2.76 Å), further suggest the formation of bonds and interactions between Pt and Mo-related species within the overgrown Pt-MoO$_{3-x}$ nanostructures.

Fig. 5 presents high-resolution Mo *3d*, S *2s*, O *1s*, and S *2p* XPS spectra for Pt-MoO$_{3-x}$ NFs | MoS$_2$, Pt-MoO$_{3-x}$ NFPs | MoS$_2$, Pt-MoO$_{3-x}$ NPs ⁝ MoS$_2$, and bulk MoS$_2$ and normalized Mo *K*-edge XANES coupled with the complementary FT-EXAFS spectra for Pt-MoO$_{3-x}$ NFs | MoS$_2$, Pt-MoO$_{3-x}$ NPs ⁝ MoS$_2$, and bulk MoS$_2$. In Fig. 5a, the high-resolution Mo *3d* XPS spectra show the assigned Mo *3d*$_{5/2}$ and Mo *3d*$_{3/2}$ doublets as Mo^{4+} (229.1–229.3 and 232.3–232.4 eV), Mo^{5+} (230.2–231.4 and 233.3–234.5 eV), and Mo^{6+} (231.5–233.2 and 234.7–236.3 eV). Interestingly, the doublet peaks at 230.2–231.4 and 233.3–234.5 eV that are ascribed to the Mo^{5+} oxidation state increase according to Pt-MoO$_{3-x}$ NPs growth on the MoS$_2$ surface. This means that oxygen-deficient MoO$_{3-x}$ nanostructures are grown on the surface of the MoS$_2$ substrate [9,36,70].

The relative amount of Mo^{5+} oxidation state further increases along with morphological transformation from Pt-MoO$_{3-x}$ NPs to Pt-MoO$_{3-x}$ NFs, also indicating that Mo^{5+} oxidation state originates from the presence of Pt-MoO$_{3-x}$ nanostructure grown on the MoS$_2$ surface. The peaks assigned to Mo^{6+} species (231.5–233.2 and 234.7–236.3 eV) for the Pt-MoO$_{3-x}$ NPs ⁝ MoS$_2$, Pt-MoO$_{3-x}$ NFPs | MoS$_2$, and Pt-MoO$_{3-x}$ NFs | MoS$_2$ samples are significantly increased compared to those for the bare bulk MoS$_2$ sample; this demonstrates that the overgrown nanostructures on the MoS$_2$ bulk surface are mixed with both MoO$_3$ and reduced MoO$_{3-x}$ phases. In addition, the peak area ratio between Mo *3d*$_{5/2}$ and Mo *3d*$_{3/2}$ changes due to the existence of Pt-MoO$_{3-x}$ nanostructures overgrown on the MoS$_2$ surface; this has also been reported for the non-stoichiometric MoO$_x$/MoS$_2$ heterostructure system [70]. For the O *1s* region, the respective deconvoluted peaks are attributed to lattice oxygen (O^{2-}; 531.5 eV), a surface hydroxyl group (OH$^-$; 532.2–532.6 eV), surface adsorbed H$_2$O or O$_2$ (533.2–533.9 eV), and O-C bonds (534.6–535.4 eV). The growth of Mo oxide nanostructures on bulk MoS$_2$ is also supported by the increase in the relative area of the lattice oxygen O^{2-} peak (Table 3). The spin-orbit splitting doublet S *2p*$_{3/2}$ (161.9–162.1 eV) and S *2p*$_{1/2}$ (163.0–163.3 eV) peaks do not show a significant difference according to the synthetic growth of Pt-MoO$_{3-x}$ nanomaterials. In addition, no shift of binding energy for the Mo *3d*$_{5/2}$, Mo *3d*$_{3/2}$, O *1s*, S *2p*$_{3/2}$, and S *2p*$_{1/2}$ peaks is observed on the bare bulk MoS$_2$ and the Pt-
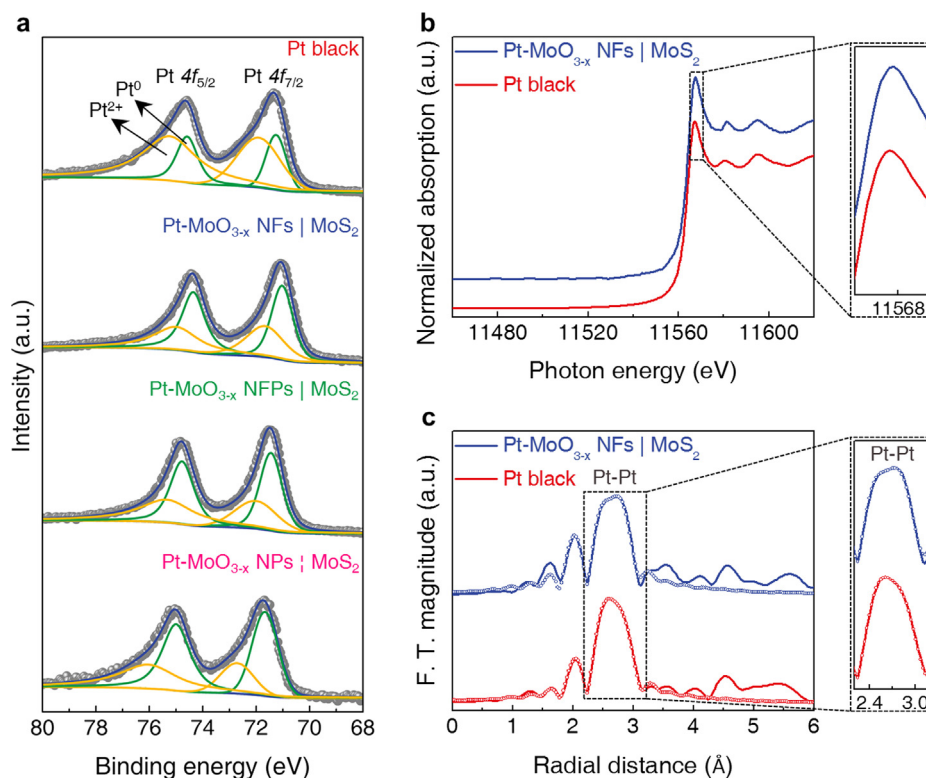
Fig. 4. Chemical and electronic analyses of Pt species in electrochemically grown Pt-MoO$_{3-x}$ nanostructures on bulk MoS$_2$ along with Pt black. (a) High-resolution XPS spectra in regions of Pt $4f$ peaks for Pt-MoO$_{3-x}$ NFs | MoS$_2$, Pt-MoO$_{3-x}$ NFPs | MoS$_2$, Pt-MoO$_{3-x}$ NPs ¦ MoS$_2$, and Pt black loaded on carbon paper electrode. (b, c) Synchrotron-based XAS analysis. Normalized Pt L_3-edge XANES (b) and magnitude of k^3-weighted FT-EXAFS spectra (c) of Pt-MoO$_{3-x}$ NFs | MoS$_2$ and Pt black loaded on carbon paper electrode. For FT-EXAFS spectra, we identify experimental and fitting results using solid lines and circle markers, respectively.

Table 1
Summary of peak assignment, binding energy, and relative area of deconvoluted peaks from high-resolution Pt $4f$ XPS spectra for electrochemically grown Pt-MoO$_{3-x}$ nanostructures on bulk MoS$_2$ along with pristine bulk MoS$_2$.

Sample	Pt $4f$		
	Peak	Binding energy (eV)	Relative area (%)
Pt black	Pt^0	71.3/74.6	28.7
	Pt^{2+}	71.9/75.2	71.3
Pt-MoO$_{3-x}$ NFs	MoS$_2$	Pt^0	71.0/74.4	56.0
	Pt^{2+}	71.7/75.0	44.0
Pt-MoO$_{3-x}$ NFPs	MoS$_2$	Pt^0	71.4/74.8	55.7
	Pt^{2+}	72.0/75.3	44.3
Pt-MoO$_{3-x}$ NPs ¦ MoS$_2$	Pt^0	71.7/75.0	60.1
	Pt^{2+}	72.7/76.0	39.9

MoO$_{3-x}$ nanostructure samples electrochemically-synthesized on bulk MoS$_2$.

In Fig. 5b and c, we illustrate the normalized Mo K-edge XANES and their correspondent FT-EXAFS spectra of Pt-MoO$_{3-x}$ NFs |

MoS$_2$, Pt-MoO$_{3-x}$ NPs ¦ MoS$_2$, and bulk MoS$_2$. The positions and shapes of the XANES spectra at the Mo K-edge are quite similar for all samples. Furthermore, the spectral white line intensity of the Mo K-absorption-edges for all analyzed samples show no significant differences (Fig. 5b). The Mo K-edge FT-EXAFS spectra are shown and compared in Fig. 5c; these spectra exhibit peaks at around 1.23, 1.99, and 2.85 Å, which are related to the Mo-O, Mo-S, and Mo-Mo distances, respectively. In accordance with the results for the Pt L_3-edge FT-EXAFS spectra provided in Fig. 4c, due to the similarity in the Pt-Pt and Mo-Mo bond distances, there are no additional metal-metal peaks in the Mo K-edge FT-EXAFS spectra for the Pt-MoO$_{3-x}$ nanostructures electrochemically overgrown on bulk MoS$_2$ [69]. Interestingly, the specific spectral peak of the Mo-O distance at around 1.23 Å for Pt-MoO$_{3-x}$ NFs | MoS$_2$ is more intense than those for the bulk MoS$_2$ and Pt-MoO$_{3-x}$ NPs ¦ MoS$_2$, confirming the existence of oxygen-deficient MoO$_{3-x}$ nanostructures grown on bulk MoS$_2$. Based on these results from diverse physicochemical analyses of the synthesized Pt-MoO$_{3-x}$ nanostructures, we demonstrate that our *in situ* electrochemical

Table 2
Summary of Pt L_3-edge EXAFS fitting results for Pt-MoO$_{3-x}$ NFs | MoS$_2$ and Pt black.

Sample	Shell	N^a	R^b (Å)	ΔE^c	σ^{2d}	R-factor^e (%)
Pt-MoO$_{3-x}$ NFs	MoS$_2$	Pt-Pt	8.96 ± 2.33	2.740 ± 0.011	3.520 ± 2.990	0.005 ± 0.001	1.67
	Pt-Mo	1.89 ± 2.73	2.695 ± 0.060	4.628 ± 10.710	0.006 ± 0.008	
Pt black	Pt-Pt	8.57 ± 0.23	2.761 ± 0.001	0.005 ± 0.000	0.005 ± 0.000	0.07

[a] Coordination number.
[b] Bond distance.
[c] Threshold energy (E_0) shift.
[d] Debye-Waller factor.
[e] R-factor is a goodness of curve fitting.

Table 3
Summary of peak assignment, binding energy, and relative area of deconvoluted peaks from high-resolution Mo 3d, S 2s, O 1s, and S 2p XPS spectra for Pt-MoO$_{3-x}$ nanostructures electrochemically grown on bulk MoS$_2$ along with pristine bulk MoS$_2$.

Sample	Mo 3d & S 2s			O 1s			S 2p		
	Peak	Binding energy (eV)	Relative area (%)	Peak	Binding energy (eV)	Relative area (%)	Peak	Binding energy (eV)	Relative area (%)
Pt-MoO$_{3-x}$ NFs | MoS$_2$	S 2s	226.7	7.2	O^{2-}	531.5	25.2	S 2p$_{3/2}$	162.0	77.6
	Mo^{4+}	229.2/232.4	53.9	OH$^-$	532.2	36.4			
	Mo^{5+}	230.2/233.3	20.5	H$_2$O or O$_2$	533.2	21.2	S 2p$_{1/2}$	163.2	22.4
	Mo^{6+}	231.5/234.7	18.4	O–C	534.6	17.2			
Pt-MoO$_{3-x}$ NFPs | MoS$_2$	S 2s	226.4	9.2	O^{2-}	531.5	20.5	S 2p$_{3/2}$	162.0	68.5
	Mo^{4+}	229.1/232.3	57.9	OH$^-$	532.3	42.9			
	Mo^{5+}	231.0/234.1	15.0	H$_2$O or O$_2$	533.4	14.0	S 2p$_{1/2}$	163.3	31.5
	Mo^{6+}	233.2/236.3	17.9	O–C	534.6	22.6			
Pt-MoO$_{3-x}$ NPs ¦ MoS$_2$	S 2 s	226.4	13.5	O^{2-}	531.5	11.3	S 2p$_{3/2}$	161.9	61.8
	Mo^{4+}	229.2/232.3	65.3	OH$^-$	532.6	44.0			
	Mo^{5+}	231.4/234.5	9.7	H$_2$O or O$_2$	533.9	9.9	S 2p$_{1/2}$	163.0	38.2
	Mo^{6+}	233.2/236.3	11.5	O–C	535.2	34.8			
Bulk MoS$_2$	S 2 s	226.5	16.0	O^{2-}	531.5	6.9	S 2p$_{3/2}$	162.1	70.3
	Mo^{4+}	229.3/232.4	74.7	OH$^-$	532.5	42.0			
	Mo^{5+}	230.7/233.8	6.5	H$_2$O or O$_2$	533.5	5.8	S 2p$_{1/2}$	163.3	29.7
	Mo^{6+}	232.4/235.5	2.8	O–C	535.4	45.3			

synthesis method can create novel nanostructures that consist of Pt and mixed Mo oxide (*i.e.* MoO$_3$ and oxygen-deficient MoO$_{3-x}$) phases.

3.4. Electrocatalytic HER performances of Pt-MoO$_{3-x}$ nanostructures

The Pt-MoO$_{3-x}$ nanostructures overgrown on bulk MoS$_2$ (Pt-MoO$_{3-x}$ NFs \| MoS$_2$, Pt-MoO$_{3-x}$ NFPs \| MoS$_2$, Pt-MoO$_{3-x}$ NPs \| MoS$_2$, and Pt-MoO$_{3-x}$ NPs ¦ MoS$_2$) were tested and evaluated as catalytic materials for electrochemical HER, in an aqueous 0.5 M H$_2$SO$_4$ electrolyte at room temperature (Fig. 6 and Tables 4 and 5). For a performance comparison, commercial Pt black with a diameter of 5 nm was also examined under the same reaction conditions (Fig. S11). From the polarization curves (Fig. 6a), the HER activity of the prepared samples can be seen to increase in the following order: bulk MoS$_2$ < Pt-MoO$_{3-x}$ NPs ¦ MoS$_2$ < Pt-MoO$_{3-x}$ NPs \| MoS$_2$ < Pt-MoO$_{3-x}$ NFPs \| MoS$_2$ < Pt-MoO$_{3-x}$ NFs \| MoS$_2$. Coupled with the activity, the HER kinetics of our catalysts follows a similar trend, as shown in the Tafel plots (Fig. 6b). Notably, in addition to the morphology effect, we believe that changes in Pt electronic states by Pt-Mo interactions, and in the amount of oxygen vacancy sites, significantly bring about the changes in Tafel slope values between Pt-MoO$_{3-x}$ NFPs and Pt-MoO$_{3-x}$ NFs. Among the tested catalytic materials, Pt-MoO$_{3-x}$ NFs \| MoS$_2$ requires an overpotential of 69 mV (*vs.* SHE) to drive a current density of −10 mA/cm^2 and shows a Tafel slope of 53 mV/dec for the HER; indeed, these values are comparable to those of commercial Pt black, which exhibits an overpotential of 62 mV and a Tafel slope of 32 mV/dec. It is worthwhile to note that our synthesized Pt-MoO$_{3-x}$ NFs \| MoS$_2$ achieves compelling HER performance—being a match for Pt black—in spite of the 10 times lower content of loaded Pt (Table 5 and Fig. S12). Since Pt-MoO$_{3-x}$ NFs \| MoS$_2$ possesses a very low amount of Pt species and the carbon paper electrode exhibits a large double layer capacitance, we were not able to find any noticeable H$_2$ adsorption-desorption peaks, which demonstrate the existence of Pt, from the CV curve recorded in 0.5 M H$_2$SO$_4$ electrolyte at room temperature. Therefore, based on ICP-OES analysis, we adopted the Pt mass activity to compare the HER activities between Pt-MoO$_{3-x}$ NFs \| MoS$_2$ and Pt black. The Pt mass activity

(current divided by Pt mass, A/mg$_{Pt}$) of the Pt-MoO$_{3-x}$ NFs \| MoS$_2$ is 2.83 A/mg$_{Pt}$ at overpotential of 100 mV (*vs.* SHE), which is 3.7 times higher than the value of 0.76 A/mg$_{Pt}$ of Pt black (Table 5). This Pt-MoO$_{3-x}$ NFs \| MoS$_2$ electrochemically generates hydrogen with a Faradaic efficiency of ~100% (Fig. 6c). Thus, we envisage that our novel *in situ* electrochemical method for synthesizing nanostructured electrocatalysts can be used to fabricate active components with ultralow Pt loading for electrochemical applications such as proton exchange membrane (PEM) fuel cells. C$_{dl}$ values for the synthesized Pt-MoO$_{3-x}$ nanostructures on bulk MoS$_2$ were obtained using CV techniques (Figs. S13, S14, S15, and S16) [49,71]. Similar to the HER activity results, the C$_{dl}$ values of the synthesized catalytic materials, which are indicative of their ECSA, increase according to the morphological transformation from Pt-MoO$_{3-x}$ NPs to Pt-MoO$_{3-x}$ NFs; the C$_{dl}$ value of Pt-MoO$_{3-x}$ NFs \| MoS$_2$ is 17.7 times greater than that of bare bulk MoS$_2$ (Table 4). As displayed in the Nyquist plots (Fig. 6d), compared to that of bulk MoS$_2$, Pt-MoO$_{3-x}$ NFs \| MoS$_2$ also demonstrates significantly decreased charge transfer resistance comparable to that of Pt black. This enhancement of the charge transfer kinetics for the HER is attributed to the distinct structural and chemical features of the Pt-MoO$_{3-x}$ nanostructures.

The outstanding HER characteristics of our novel catalytic materials can be ascribed to their three distinctive physicochemical properties related to both formation and subsequent morphological changes of Pt-MoO$_{3-x}$ nanostructures overgrown on the bulk MoS$_2$ surface. The first is the creation of novel interfaces between Pt and Mo oxides in the overgrown Pt-MoO$_{3-x}$ nanostructures. Based on the results of HAADF-STEM, EDS elemental mapping, XPS, XANES, and EXAFS analyses, shown in Figs. 3–5, we confirm the combination between Pt and Mo oxides in the electrochemically synthesized nanostructures, thereby demonstrating the formation of Pt-Mo oxides interfacial sites. These newly formed interfaces can be novel HER active sites enabled by synergistic interactions between Pt and Mo oxides, ultimately contributing to the enhancement of electrocatalytic HER performance. The second is the non-stoichiometry of MoO$_{3-x}$ originating from oxygen vacancies. It has been reported that oxygen vacancy sites on the surface of Mo oxides can promote the adsorption of oxygen-containing species (*i.e.* oxygenates), and therefore the oxygen
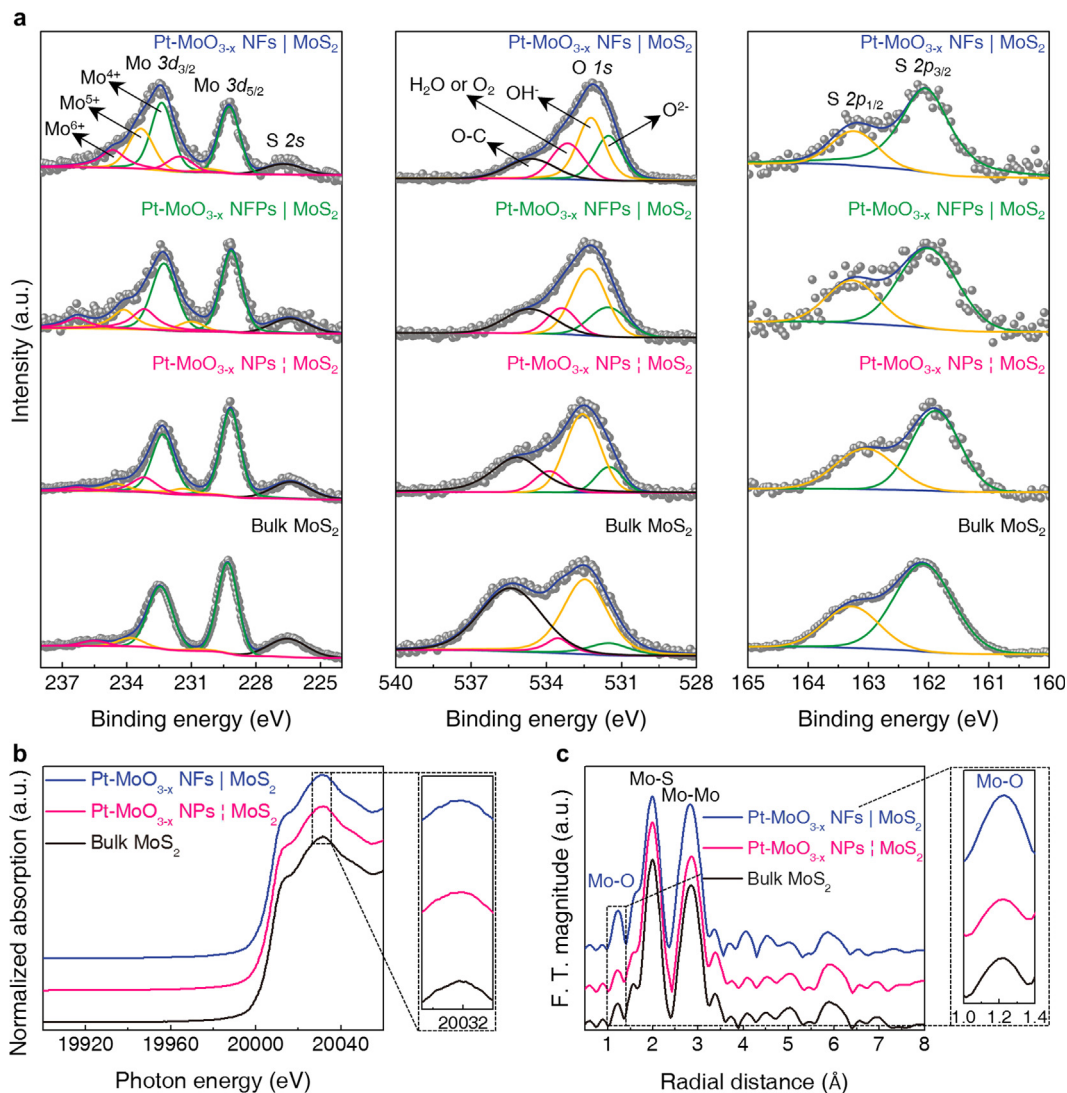
Fig. 5. Chemical and electronic analyses of Mo, O, and S species in electrochemically grown Pt-MoO_{3-x} nanostructures on bulk MoS_2 along with pristine bulk MoS_2. (a) High-resolution XPS spectra in the regions of Mo 3d, S 2s, O 1s, and S 2p peaks for Pt-MoO_{3-x} NFs | MoS_2, Pt-MoO_{3-x} NFPs | MoS_2, Pt-MoO_{3-x} NPs ¦ MoS_2, and bulk MoS_2 loaded on carbon paper electrode. (b, c) Synchrotron-based XAS analysis. Normalized Mo K-edge XANES (b) and magnitude of k^3-weighted FT-EXAFS spectra (c) of Pt-MoO_{3-x} NFs | MoS_2, Pt-MoO_{3-x} NPs ¦ MoS_2, and bulk MoS_2 loaded on carbon paper electrode.

vacancy sites can be beneficial for catalytic reactions such as the biomass deoxygenation reaction and hydrogen evolution reaction [36,72]. In particular, oxygen vacancy sites such as Mo^{5+} promote the adsorption of oxygenates such as H_3O^+ on metal oxide surfaces, and therefore can serve as novel active sites for HER in acidic environments [36]. The existence and increase of the Mo^{5+} oxidation state in our prepared nanostructured Pt-MoO_{3-x} samples were confirmed by XPS analyses (Fig. 5a) and discussed. The formation of oxygen vacancies in orthorhombic α-MoO_3 also leads to expanded interlayer distance, which can expedite insertion/removal processes of H^+ and other small ions into/from the lattice in MoO_{3-x} [9,73]. In addition, introducing oxygen vacancies into metal oxides enhances the electrical conductivity because oxygen vacancies serve as shallow donors and therefore bring about band-gap narrowing [9,36,73,74]. The last prominent feature is perhaps related to the change and increase of ECSA of the electrochemically-synthesized Pt-MoO_{3-x} nanostructures on the bulk MoS_2 surface. Morphological analysis using SEM and TEM (Figs. 2 and 3) demonstrated that the prepared Pt-MoO_{3-x} NF structures are composed of randomly oriented Pt-MoO_{3-x} building

blocks with nanometer size. Furthermore, compared to the C_{dl} value of bulk MoS_2 (0.10 mF/cm^2), the significantly increased C_{dl} value of Pt-MoO_{3-x} NFs | MoS_2 (1.77 mF/cm^2) indicates that Pt-MoO_{3-x} NF structures may possess a higher number of catalytic active sites and improved ability to exchange ions between electrolyte and their active sites for electrocatalytic HER [49,71]. However, we should perform further studies on the detailed explanation of the effect of Pt-Mo interactions on creating novel HER active sites through additional control experiments.

The electrocatalytic stability is also a major issue for catalytic materials. To measure the HER stability in an acidic environment, a long-term chronopotentiometry test was performed by obtaining potential profiles with reaction time of 100 h at constant HER current density of −10 mA/cm^2 in a 0.5 M H_2SO_4. As shown in Fig. 6e, the tested samples, including commercial Pt black, Pt-MoO_{3-x} NFPs | MoS_2, and Pt-MoO_{3-x} NFs | MoS_2, maintained the initial potential value at −10 mA/cm^2 during 100 h of continuous operation, demonstrating the good stability of our prepared Pt-MoO_{3-x} nanostructure materials. After the stability test, the re-measured polarization curve of Pt-MoO_{3-x} NFs | MoS_2 also indicates that
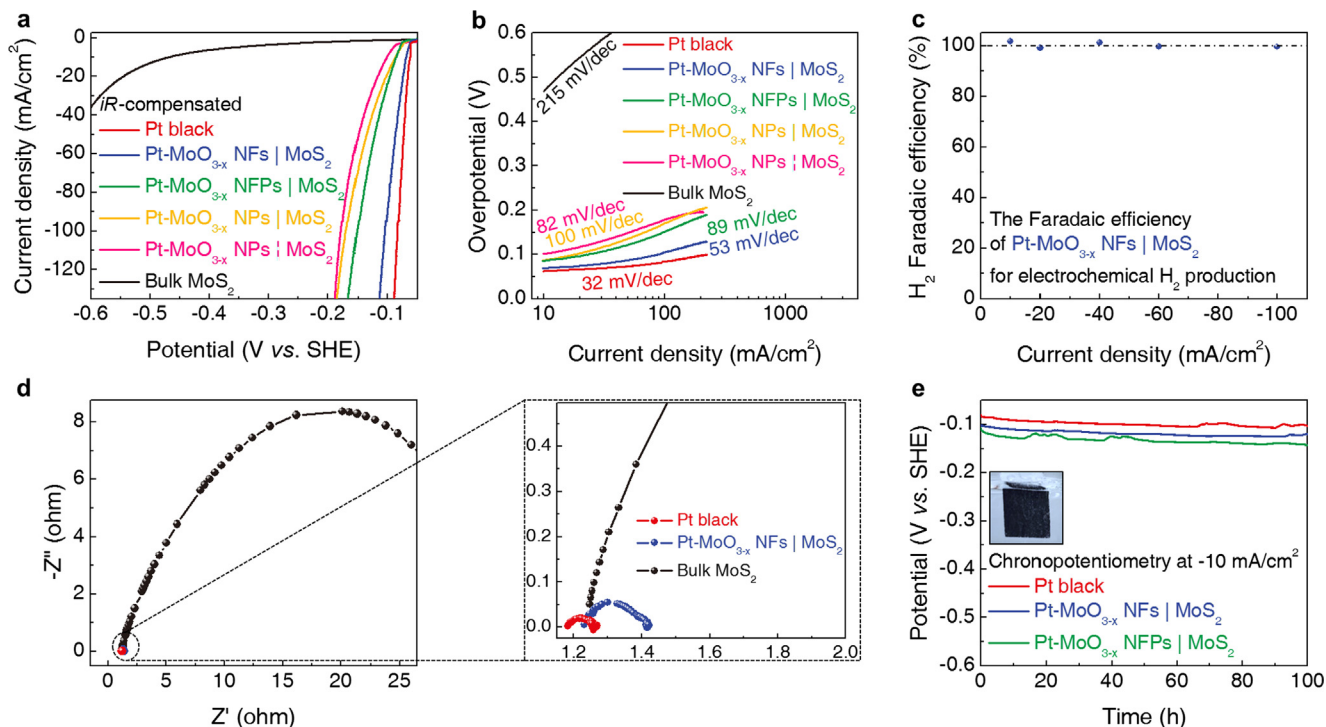
Fig. 6. Electrochemical performance analysis of Pt-MoO$_{3-x}$ nanostructures electrochemically grown on bulk MoS$_2$ surface toward electrocatalytic HER in 0.5 M H$_2$SO$_4$ electrolyte. (a) iR-compensated polarization curves for Pt black, Pt-MoO$_{3-x}$ NFs | MoS$_2$, Pt-MoO$_{3-x}$ NFPs | MoS$_2$, Pt-MoO$_{3-x}$ NPs | MoS$_2$, Pt-MoO$_{3-x}$ NPs ¦ MoS$_2$, and bulk MoS$_2$ loaded on carbon paper electrode. (b) Tafel plots derived from polarization curves in (a). Note that estimated Tafel slopes are labeled. (c) H$_2$ Faradaic efficiency of Pt-MoO$_{3-x}$ NFs | MoS$_2$ as a function of current density. (d) Nyquist plots of Pt black, Pt-MoO$_{3-x}$ NFs | MoS$_2$, and bulk MoS$_2$. (e) Chronopotentiometry results for Pt black, Pt-MoO$_{3-x}$ NFs | MoS$_2$, and Pt-MoO$_{3-x}$ NFPs | MoS$_2$ samples. Inset digital photograph presents hydrogen bubbles generated from Pt-MoO$_{3-x}$ NFs | MoS$_2$ loaded on carbon paper electrode during chronopotentiometry experiment.

Table 4
Summary of properties of electrochemically grown Pt-MoO$_{3-x}$ nanostructure samples as HER electrocatalysts.

Sample	Overpotential (mV vs. SHE) at 10 mA/cm^2	Tafel slope (mv/dec)	C$_{dl}$ (mF/cm^2)
Pt-MoO$_{3-x}$ NFs	MoS$_2$	69	53	1.77
Pt-MoO$_{3-x}$ NFPs	MoS$_2$	86	89	1.34
Pt-MoO$_{3-x}$ NPs	MoS$_2$	87	100	1.03
Pt-MoO$_{3-x}$ NPs ¦ MoS$_2$	101	82	0.87
Bulk MoS$_2$	468	215	0.10

there is a small difference but no significant increase of the overpotential value at −10 mA/cm^2 (Fig. S17). Furthermore, the SEM images from Pt-MoO$_{3-x}$ NFs | MoS$_2$ loaded onto a carbon paper electrode after the stability test suggest that there is no severe structural deformation of the synthesized Pt-MoO$_{3-x}$ nanostructures for the entire chronopotentiometry test in acidic environment (Fig. S17). These results suggest that the novel electrochemical synthesis method suggested in this work can be widely used to design and develop high performance, stable Pt and Mo-based electrocatalysts with 2D layered structures.

3.5. Computational examination of why Pt-MoO$_{3-x}$ nanostructures are efficient for HER

On the basis of the results from various physicochemical characterizations and electrochemical performance analyses, we additionally conducted computational investigation to expand on the excellent HER abilities of the synthesized Pt-MoO$_{3-x}$ nanostructures. In this work, we performed DFT calculations on model surface structures containing different components of Pt-MoO$_{3-x}$ nanostructures to understand why the Pt-MoO$_{3-x}$ nanostructures show good HER performance. As shown in Fig. 7, by optimizing through DFT calculations, we prepared Pt(1 1 1) and MoO$_3$(0 1 0) surfaces and their mixed Pt-MoO$_3$ surfaces, and generated defect sites on MoO$_3$-containing surfaces to fabricate other surfaces including MoO$_{3-x}$ structures: the created surface structures were Pt(1 1 1), MoO$_3$(0 1 0), Pt-MoO$_3$, oxygen-deficient MoO$_3$ (MoO$_{3-x}$), and Pt-MoO$_{3-x}$. In detail, to create oxygen vacancy defects on MoO$_3$(0 1 0) surface structures, we removed an oxygen atom at the gap between two MoO$_3$ layers that were interacting via van der Waals forces due to the lowest formation enthalpy for this defect site (Fig. 7d). Furthermore, for the mixed Pt-MoO$_3$ surfaces, we considered two defect sites at the boundary between MoO$_3$ and Pt (Fig. 7e) or MoO$_3$ surface (Fig. 7f). These fabricated surface struc-

Table 5
Comparison of electrocatalytic HER kinetics between synthesized Pt-MoO$_{3-x}$ NFs | MoS$_2$ and commercial Pt black catalyst.

Sample	Pt loading amount[a] (mg$_{Pt}$/cm^2)	Mass activity[b] (A/mg$_{Pt}$)	Overpotential[c] (mV vs. SHE)	Tafel slope (mv/dec)
Pt-MoO$_{3-x}$ NFs	MoS$_2$	0.03	2.83	69	53
Pt black	0.3	0.76	62	32

[a] Mass of Pt per unit area of carbon paper electrode was estimated based on ICP-OES results.
[b] Pt mass activity was calculated at overpotential of 100 mV (vs. SHE).
[c] Overpotential was measured at current density of 10 mA/cm^2.
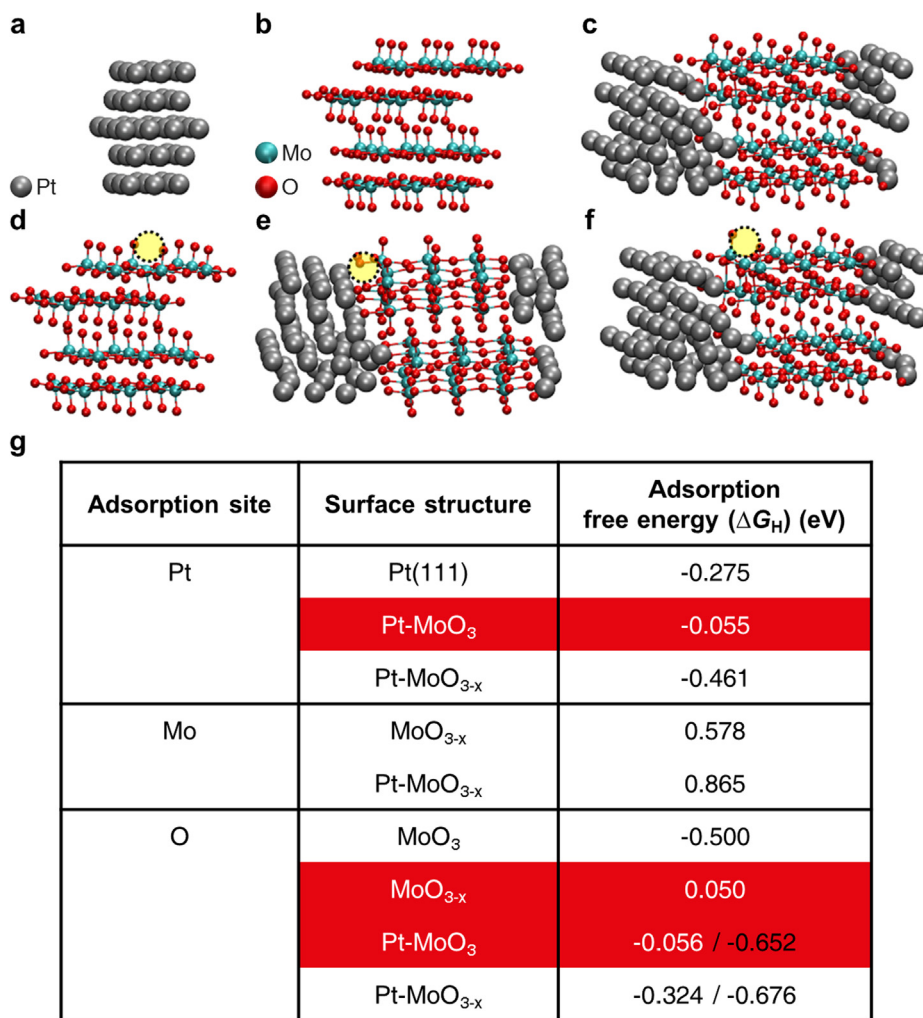
Fig. 7. Surface structures optimized from DFT calculations and their hydrogen adsorption free energy. (a, b, c, e, d, f) Simulated structures for Pt(1 1 1) (a), MoO_3(0 1 0) (b), Pt and MoO_3 (c), MoO_3 with oxygen vacancy defect (d), and Pt and MoO_3 with oxygen vacancy defect (e, f). Note that oxygen defect sites are highlighted using yellow circles. g, Summary of adsorption free energy (ΔG_H) of a hydrogen atom. Note that favorable adsorption sites for hydrogen atoms and corresponding ΔG_H values are highlighted in red and white.

tures are displayed from a different point of view in Fig. S18. It is worthwhile to note that we assessed the electrocatalytic HER activities of each DFT-optimized surface structure according to the corresponding adsorption free energies (ΔG_H) of hydrogen atoms on the model surface structures. For all of the created surface structures, we found several adsorption sites for hydrogen atoms, and calculated the ΔG_H of a hydrogen atom being on these different adsorption sites from model surface structures, as summarized in Fig. 7g. Along with the derived ΔG_H values, we also show diverse configurations of hydrogen atoms on adsorption sites (i.e. Pt, Mo, and O) from the optimized surface structures (Figs. S19, S20, and S21). It is well-known that a surface structure that bears good catalytic activities toward HER should adsorb hydrogen atoms with low energy barrier and energy loss. If the surface possesses a large negative or positive ΔG_H value, high overpotential will be required to detach or attach a hydrogen atom during electrocatalytic HER [29]. Interestingly, there are some favorable adsorption sites in our model surface structures that show small absolute values of ΔG_H less than 0.1 eV: (i) Pt (ΔG_H = −0.055 eV, Fig. S21b) and (ii) O (ΔG_H = −0.056 eV, Fig. S19b) sites at the boundary between Pt and MoO_3 in the Pt-MoO_3 surface structure, and (iii) O atom (ΔG_H = 0.050 eV, Fig. S19d) from the oxygen-deficient MoO_{3-x} surface structure can contribute to accelerate

the electrocatalytic HER over Pt-MoO_{3-x} nanostructures overgrown on bulk MoS_2. Confirming our hypothesis derived from the correlation between the physicochemical properties of Pt-MoO_{3-x} nanostructures and their outstanding HER performance, these computational investigation results indicate that the creation of Pt and O atoms at the Pt-MoO_3 interfaces, and O sites at the MoO_{3-x} surfaces, will boost the electrocatalytic HER performance of the Pt-MoO_{3-x} nanostructures overgrown on bulk MoS_2.

4. Conclusion

In summary, we have developed a new in situ electrochemical synthesis technique for Pt-MoO_{3-x} nanostructures grown on commercial bulk MoS_2 material. The Pt-MoO_{3-x} NF and/or NP structures overgrown on bulk MoS_2 substrate were easily prepared and controlled by applying electrical energy to the bulk MoS_2 and using Pt counter dissolution in an acid solution. Among the prepared catalytic materials, Pt-MoO_{3-x} NFs | MoS_2 showed an overpotential of 69 mV (vs. SHE) at −10 mA/cm^2 and a Tafel slope of 53 mV/dec for the electrocatalytic HER. Moreover, in comparison with the Pt mass activity (0.76 A/mg$_{Pt}$) of conventional Pt black at its overpotential of 100 mV (vs. SHE), Pt-MoO_{3-x} NFs | MoS_2 demonstrated a 3.7 times greater Pt mass activity value of

2.83 A/mg$_{Pt}$. The creation of Pt and MoO$_3$ interfacial sites and the existence of more oxygen vacancy sites such as Mo^{5+} in the Pt-MoO$_{3-x}$ NFs | MoS$_2$ were responsible for the significantly improved electrochemical HER performance. Our DFT calculations also demonstrated that Pt and O sites at the Pt and MoO$_3$ interfaces and O sites at the defective MoO$_{3-x}$ in the Pt-MoO$_{3-x}$ NFs | MoS$_2$ show hydrogen adsorption free energy low enough to promote the HER. Future work will require in-depth analysis of the overgrowth mechanism of the Pt-MoO$_{3-x}$ nanostructure on commercial bulk MoS$_2$, and the detailed understanding of Pt-Mo interactions as the HER active sites with some control experiments. Nevertheless, our methodology for preparing Pt-MoO$_{3-x}$ nanostructure presented herein is expected to provide a useful way to generate new HER active sites on 2D layered structures such as transition-metal dichalcogenides and oxide materials. This synthetic approach can also be a promising method to use only solid phase materials such as Pt wire and MoS$_2$ powder, without need for expensive precious metal salts (*e.g.* H$_2$PtCl$_6$), for preparing electro-catalytic materials.

Declaration of Competing Interest

Hyung Ju Kim and Daewon Lee are authors on a patent application related to this work held by the Korea Research Institute of Chemical Technology (KRICT) (no. PCT/KR2018/005783, applied 21 05 18).

Acknowledgements

Appendix A. Supplementary material

Supplementary data to this article can be found online at https://doi.org/10.1016/j.jcat.2019.10.027.

References

[1] T.F. Jaramillo, K.P. Jørgensen, J. Bonde, J.H. Nielsen, S. Horch, I. Chorkendorff, Identification of active edge sites for electrochemical H2 evolution from MoS2 nanocatalysts, Science 317 (2007) 100–102, https://doi.org/10.1126/science.1141483.

[2] L.Q. Mai, B. Hu, W. Chen, Y.Y. Qi, C.S. Lao, R.S. Yang, Y. Dai, Z.L. Wang, Lithiated MoO3 nanobelts with greatly improved performance for lithium batteries, Adv. Mater. 19 (2007) 3712–3716, https://doi.org/10.1002/adma.200700883.

[3] T. Brezesinski, J. Wang, S.H. Tolbert, B. Dunn, Ordered mesoporous α-MoO3 with iso-oriented nanocrystalline walls for thin-film pseudocapacitors, Nat. Mater. 9 (2010) 146–151, https://doi.org/10.1038/nmat2612.

[4] B. Radisavljevic, A. Radenovic, J. Brivio, V. Giacometti, A. Kis, Single-layer MoS2 transistors, Nat. Nanotechnol. 6 (2011) 147–150, https://doi.org/10.1038/nnano.2010.279.

[5] G. Jin, W. Weng, Z. Lin, N.F. Dummer, S.H. Taylor, C.J. Kiely, J.K. Bartley, G.J. Hutchings, Fe2(MoO4)3/MoO3 nano-structured catalysts for the oxidation of methanol to formaldehyde, J. Catal. 296 (2012) 55–64, https://doi.org/10.1016/j.jcat.2012.09.001.

[6] W. Tang, Y. Zhu, Y. Hou, L. Liu, Y. Wu, K.P. Loh, H. Zhang, K. Zhu, Aqueous rechargeable lithium batteries as an energy storage system of superfast charging, Energy Environ. Sci. 6 (2013) 2093–2104, https://doi.org/10.1039/C3EE24249H.

[7] S. Triwahyono, A.A. Jalil, N.N. Ruslan, H.D. Setiabudi, N.H.N. Kamarudin, C5–C7 linear alkane hydroisomerization over MoO3–ZrO2 and Pt/MoO3–ZrO2 catalysts, J. Catal. 303 (2013) 50–59, https://doi.org/10.1016/j.jcat.2013.03.016.

[8] Z. Zhang, J. Liu, J. Gu, L. Su, L. Cheng, An overview of metal oxide materials as electrocatalysts and supports for polymer electrolyte fuel cells, Energy Environ. Sci. 7 (2014) 2535–2558, https://doi.org/10.1039/C3EE43886D.

[9] H.-S. Kim, J.B. Cook, H. Lin, Jesse S. Ko, Sarah H. Tolbert, V. Ozolins, B. Dunn, Oxygen vacancies enhance pseudocapacitive charge storage properties of MoO3−x, Nat. Mater. 16 (2016) 454–460, https://doi.org/10.1038/nmat4810.

[10] Y.-C. Chen, A.-Y. Lu, P. Lu, X. Yang, C.-M. Jiang, M. Mariano, B. Kaehr, O. Lin, A. Taylor, I.D. Sharp, L.-J. Li, S.S. Chou, V. Tung, Structurally deformed MoS2 for electrochemically stable, thermally resistant, and highly efficient hydrogen evolution reaction, Adv. Mater. 29 (2017) 1703863, https://doi.org/10.1002/adma.201703863.

[11] L. Xie, M. Liao, S. Wang, H. Yu, L. Du, J. Tang, J. Zhao, J. Zhang, P. Chen, X. Lu, G. Wang, G. Xie, R. Yang, D. Shi, G. Zhang, Graphene-contacted ultrashort channel monolayer MoS2 transistors, Adv. Mater. 29 (2017) 1702522, https://doi.org/10.1002/adma.201702522.

[12] S. Zhang, G. Wang, J. Jin, L. Zhang, Z. Wen, J. Yang, Self-catalyzed decomposition of discharge products on the oxygen vacancy sites of MoO3 nanosheets for low-overpotential Li-O2 batteries, Nano Energy 36 (2017) 186–196, https://doi.org/10.1016/j.nanoen.2017.04.038.

[13] K. Murugappan, E.M. Anderson, D. Teschner, T.E. Jones, K. Skorupska, Y. Román-Leshkov, Operando NAP-XPS unveils differences in MoO3 and Mo2C during hydrodeoxygenation, Nat. Catal. 1 (2018) 960–967, https://doi.org/10.1038/s41929-018-0171-9.

[14] N. Huang, R. Peng, Y. Ding, S. Yan, G. Li, P. Sun, X. Sun, X. Liu, H. Yu, Facile chemical-vapour-deposition synthesis of vertically aligned co-doped MoS2 nanosheets as an efficient catalyst for triiodide reduction and hydrogen evolution reaction, J. Catal. 373 (2019) 250–259, https://doi.org/10.1016/j.jcat.2019.04.007.

[15] K.-D. Kim, Y.-K. Lee, Active phase of dispersed MoS2 catalysts for slurry phase hydrocracking of vacuum residue, J. Catal. 369 (2019) 111–121, https://doi.org/10.1016/j.jcat.2018.10.013.

[16] S. Yang, Y. Wang, H. Zhang, Y. Zhang, L. Liu, L. Fang, X. Yang, X. Gu, Y. Wang, Unique three-dimensional Mo2C@MoS2 heterojunction nanostructure with S vacancies as outstanding all-pH range electrocatalyst for hydrogen evolution, J. Catal. 371 (2019) 20–26, https://doi.org/10.1016/j.jcat.2019.01.020.

[17] Q.H. Wang, K. Kalantar-Zadeh, A. Kis, J.N. Coleman, M.S. Strano, Electronics and optoelectronics of two-dimensional transition metal dichalcogenides, Nat. Nanotechnol. 7 (2012) 699–712, https://doi.org/10.1038/nnano.2012.193.

[18] D. Jariwala, T.J. Marks, M.C. Hersam, Mixed-dimensional van der Waals heterostructures, Nat. Mater. 16 (2016) 170–181, https://doi.org/10.1038/nmat4703.

[19] J. Kibsgaard, Z. Chen, B.N. Reinecke, T.F. Jaramillo, Engineering the surface structure of MoS2 to preferentially expose active edge sites for electrocatalysis, Nat. Mater. 11 (2012) 963–969, https://doi.org/10.1038/nmat3439.

[20] O. Lopez-Sanchez, D. Lembke, M. Kayci, A. Radenovic, A. Kis, Ultrasensitive photodetectors based on monolayer MoS2, Nat. Nanotechnol. 8 (2013) 497–501, https://doi.org/10.1038/nnano.2013.100.

[21] M. Acerce, D. Voiry, M. Chhowalla, Metallic 1T phase MoS2 nanosheets as supercapacitor electrode materials, Nat. Nanotechnol. 10 (2015) 313–318, https://doi.org/10.1038/nnano.2015.40.

[22] H. Li, C. Tsai, A.L. Koh, L. Cai, A.W. Contryman, A.H. Fragapane, J. Zhao, H.S. Han, H.C. Manoharan, F. Abild-Pedersen, J.K. Nørskov, X. Zheng, Activating and optimizing MoS2 basal planes for hydrogen evolution through the formation of strained sulphur vacancies, Nat. Mater. 15 (2015) 48–53, https://doi.org/10.1038/nmat4465.

[23] T. An, Y. Wang, J. Tang, W. Wei, X. Cui, A.M. Alenizi, L. Zhang, G. Zheng, Interlaced NiS2–MoS2 nanoflake-nanowires as efficient hydrogen evolution electrocatalysts in basic solutions, J. Mater. Chem. A 4 (2016) 13439–13443, https://doi.org/10.1039/C6TA05022K.

[24] R. Dai, A. Zhang, Z. Pan, A.M. Al-Enizi, A.A. Elzatahry, L. Hu, G. Zheng, Epitaxial growth of lattice-mismatched core-shell TiO2@MoS2 for enhanced lithium-ion storage, Small 12 (2016) 2792–2799, https://doi.org/10.1002/smll.201600237.

[25] J.-W. Jung, W.-H. Ryu, S. Yu, C. Kim, S.-H. Cho, I.-D. Kim, Dimensional effects of MoS2 nanoplates embedded in carbon nanofibers for bifunctional li and na insertion and conversion reactions, ACS Appl. Mater. Interfaces 8 (2016) 26758–26768, https://doi.org/10.1021/acsami.6b08267.

[26] C. Bae, T.A. Ho, H. Kim, S. Lee, S. Lim, M. Kim, H. Yoo, J.M. Montero-Moreno, J.H. Park, H. Shin, Bulk layered heterojunction as an efficient electrocatalyst for hydrogen evolution, Sci. Adv. 3 (2017), https://doi.org/10.1126/sciadv.1602215 e1602215.

[27] Z. Deng, H. Jiang, Y. Hu, Y. Liu, L. Zhang, H. Liu, C. Li, 3D ordered macroporous MoS2@C nanostructure for flexible Li-Ion batteries, Adv. Mater. 29 (2017) 1603020, https://doi.org/10.1002/adma.201603020.

[28] S. Park, J. Park, H. Abroshan, L. Zhang, J.K. Kim, J. Zhang, J. Guo, S. Siahrostami, X. Zheng, Enhancing catalytic activity of MoS2 basal plane S-vacancy by co cluster addition, ACS Energy Lett. 3 (2018) 2685–2693, https://doi.org/10.1021/acsenergylett.8b01567.

[29] B. Hinnemann, P.G. Moses, J. Bonde, K.P. Jørgensen, J.H. Nielsen, S. Horch, I. Chorkendorff, J.K. Nørskov, Biomimetic hydrogen evolution: MoS2 nanoparticles as catalyst for hydrogen evolution, J. Am. Chem. Soc. 127 (2005) 5308–5309, https://doi.org/10.1021/ja0504690.

[30] Y. Li, H. Wang, L. Xie, Y. Liang, G. Hong, H. Dai, MoS2 Nanoparticles grown on graphene: an advanced catalyst for the hydrogen evolution reaction, J. Am. Chem. Soc. 133 (2011) 7296–7299, https://doi.org/10.1021/ja201269b.

[31] D. Voiry, M. Salehi, R. Silva, T. Fujita, M. Chen, T. Asefa, V.B. Shenoy, G. Eda, M. Chhowalla, Conducting MoS2 nanosheets as catalysts for hydrogen evolution reaction, Nano Lett. 13 (2013) 6222–6227, https://doi.org/10.1021/nl403661s.

[32] H. Wang, Z. Lu, D. Kong, J. Sun, T.M. Hymel, Y. Cui, Electrochemical tuning of MoS2 nanoparticles on three-dimensional substrate for efficient hydrogen evolution, ACS Nano 8 (2014) 4940–4947, https://doi.org/10.1021/nn500959v.

[33] Y. Kim, D.H.K. Jackson, D. Lee, M. Choi, T.-W. Kim, S.-Y. Jeong, H.-J. Chae, H.W. Kim, N. Park, H. Chang, T.F. Kuech, H.J. Kim, In situ electrochemical activation of atomic layer deposition coated MoS2 basal planes for efficient hydrogen evolution reaction, Adv. Funct. Mater. 27 (2017) 1701825, https://doi.org/10.1002/adfm.201701825.

[34] S.-Q. Wang, X. Cai, Y. Song, X. Sun, X.-X. Liu, VOx@MoO3 nanorod composite for high-performance supercapacitors, Adv. Funct. Mater. 28 (2018) 1803901, https://doi.org/10.1002/adfm.201803901.

[35] G. Qu, J. Wang, G. Liu, B. Tian, C. Su, Z. Chen, J.-P. Rueff, Z. Wang, Vanadium doping enhanced electrochemical performance of molybdenum oxide in lithium-ion batteries, Adv. Funct. Mater. 29 (2019) 1805227, https://doi.org/10.1002/adfm.201805227.

[36] Z. Luo, R. Miao, T.D. Huan, I.M. Mosa, A.S. Poyraz, W. Zhong, J.E. Cloud, D.A. Kriz, S. Thanneeru, J. He, Y. Zhang, R. Ramprasad, S.L. Suib, Mesoporous MoO3–x material as an efficient electrocatalyst for hydrogen evolution reactions, Adv. Energy Mater. 6 (2016) 1600528, https://doi.org/10.1002/aenm.201600528.

[37] R.S. Datta, F. Haque, M. Mohiuddin, B.J. Carey, N. Syed, A. Zavabeti, B. Zhang, H. Khan, K.J. Berean, J.Z. Ou, N. Mahmood, T. Daeneke, K. Kalantar-zadeh, Highly active two dimensional α-MoO3–x for the electrocatalytic hydrogen evolution reaction, J. Mater. Chem. A 5 (2017) 24223–24231, https://doi.org/10.1039/C7TA07705J.

[38] S.T. Hunt, M. Milina, A.C. Alba-Rubio, C.H. Hendon, J.A. Dumesic, Y. Román-Leshkov, Self-assembly of noble metal monolayers on transition metal carbide nanoparticle catalysts, Science 352 (2016) 974–978, https://doi.org/10.1126/science.aad8471.

[39] Y. Luo, D. Huang, M. Li, X. Xiao, W. Shi, M. Wang, J. Su, Y. Shen, MoS2 nanosheet decorated with trace loads of Pt as highly active electrocatalyst for hydrogen evolution reaction, Electrochim. Acta 219 (2016) 187–193, https://doi.org/10.1016/j.electacta.2016.09.151.

[40] J. Zhang, T. Wang, L. Liu, K. Du, W. Liu, Z. Zhu, M. Li, Molybdenum disulfide and Au ultrasmall nanohybrids as highly active electrocatalysts for hydrogen evolution reaction, J. Mater. Chem. A 5 (2017) 4122–4128, https://doi.org/10.1039/C6TA10385E.

[41] S. Li, J.K. Lee, S. Zhou, M. Pasta, J.H. Warner, Synthesis of surface grown Pt nanoparticles on edge-enriched MoS2 porous thin films for enhancing electrochemical performance, Chem. Mater. 31 (2019) 387–397, https://doi.org/10.1021/acs.chemmater.8b03540.

[42] X. Huang, Z. Zeng, S. Bao, M. Wang, X. Qi, Z. Fan, H. Zhang, Solution-phase epitaxial growth of noble metal nanostructures on dispersible single-layer molybdenum disulfide nanosheets, Nat. Commun. 4 (2013) 1444, https://doi.org/10.1038/ncomms2472.

[43] J. Deng, H. Li, J. Xiao, Y. Tu, D. Deng, H. Yang, H. Tian, J. Li, P. Ren, X. Bao, Triggering the electrocatalytic hydrogen evolution activity of the inert two-dimensional MoS2 surface via single-atom metal doping, Energy Environ. Sci. 8 (2015) 1594–1601, https://doi.org/10.1039/C5EE00751H.

[44] K. Qi, S. Yu, Q. Wang, W. Zhang, J. Fan, W. Zheng, X. Cui, Decoration of the inert basal plane of defect-rich MoS2 with Pd atoms for achieving Pt-similar HER activity, J. Mater. Chem. A 4 (2016) 4025–4031, https://doi.org/10.1039/C5TA10337A.

[45] H. Zhang, Y. Wang, E.R. Fachini, C.R. Cabrera, Electrochemically codeposited platinum/molybdenum oxide electrode for catalytic oxidation of methanol in acid solution, Electrochem. Solid-State Lett. 2 (1999) 437–439, https://doi.org/10.1149/1.1390863.

[46] L. Ma, X. Zhao, F. Si, C. Liu, J. Liao, L. Liang, W. Xing, A comparative study of Pt/C and Pt–MoOx/C catalysts with various compositions for methanol electro-oxidation, Electrochim. Acta 55 (2010) 9105–9112, https://doi.org/10.1016/j.electacta.2010.08.034.

[47] E. Gottlieb, M. Kopeć, M. Banerjee, J. Mohin, D. Yaron, K. Matyjaszewski, T. Kowalewski, In-situ platinum deposition on nitrogen-doped carbon films as a source of catalytic activity in a hydrogen evolution reaction, ACS Appl. Mater. Interfaces 8 (2016) 21531–21538, https://doi.org/10.1021/acsami.6b03924.

[48] L. Ji, J. Wang, S. Zuo, Z. Chen, In situ preparation of Pt nanoparticles supported on N-doped carbon as highly efficient electrocatalysts for hydrogen production, J. Phys. Chem. C 121 (2017) 8923–8930, https://doi.org/10.1021/acs.jpcc.7b01447.

[49] G. Liu, Y. Qiu, Z. Wang, J. Zhang, X. Chen, M. Dai, D. Jia, Y. Zhou, Z. Li, P. Hu, Efficiently synergistic hydrogen evolution realized by trace amount of Pt-decorated defect-rich SnS2 nanosheets, ACS Appl. Mater. Interfaces 9 (2017) 37750–37759, https://doi.org/10.1021/acsami.7b11413.

[50] M. Tavakkoli, N. Holmberg, R. Kronberg, H. Jiang, J. Sainio, E.I. Kauppinen, T. Kallio, K. Laasonen, Electrochemical activation of single-walled carbon nanotubes with pseudo-atomic-scale platinum for the hydrogen evolution reaction, ACS Catal. 7 (2017) 3121–3130, https://doi.org/10.1021/acscatal.7b00199.

[51] X. Shang, B. Dong, Y.-M. Chai, C.-G. Liu, In-situ electrochemical activation designed hybrid electrocatalysts for water electrolysis, Sci. Bull. 63 (2018) 853–876, https://doi.org/10.1016/j.scib.2018.05.014.

[52] K. Tang, X. Wang, Q. Li, C. Yan, High edge selectivity of in situ electrochemical Pt deposition on edge-rich layered WS2 nanosheets, Adv. Mater. 30 (2018) 1704779, https://doi.org/10.1002/adma.201704779.

[53] J. Zhang, Y. Zhao, X. Guo, C. Chen, C.-L. Dong, R.-S. Liu, C.-P. Han, Y. Li, Y. Gogotsi, G. Wang, Single platinum atoms immobilized on an MXene as an efficient catalyst for the hydrogen evolution reaction, Nat. Catal. 1 (2018) 985–992, https://doi.org/10.1038/s41929-018-0195-1.

[54] G. Kresse, J. Furthmüller, Efficient iterative schemes for ab initio total-energy calculations using a plane-wave basis set, Phys. Rev. B 54 (1996) 11169–11186, https://doi.org/10.1103/PhysRevB.54.11169.

[55] G. Kresse, D. Joubert, From ultrasoft pseudopotentials to the projector augmented-wave method, Phys. Rev. B 59 (1999) 1758–1775, https://doi.org/10.1103/PhysRevB.59.1758.

[56] J. Klimeš, D.R. Bowler, A. Michaelides, Chemical accuracy for the van der Waals density functional, J. Phys.: Condens. Matter 22 (2009) 022201–022205, https://doi.org/10.1088/0953-8984/22/2/022201.

[57] J. Klimeš, D.R. Bowler, A. Michaelides, Van der Waals density functionals applied to solids, Phys. Rev. B 83 (2011) 195131–195143, https://doi.org/10.1103/PhysRevB.83.195131.

[58] J.K. Nørskov, T. Bligaard, A. Logadottir, J.R. Kitchin, J.G. Chen, S. Pandelov, U. Stimming, Trends in the exchange current for hydrogen evolution, J. Electrochem. Soc. 152 (2005) J23–J26, https://doi.org/10.1149/1.1856988.

[59] G. Dong, M. Fang, H. Wang, S. Yip, H.-Y. Cheung, F. Wang, C.-Y. Wong, S.T. Chu, J.C. Ho, Insight into the electrochemical activation of carbon-based cathodes for hydrogen evolution reaction, J. Mater. Chem. A 3 (2015) 13080–13086, https://doi.org/10.1039/C5TA02551F.

[60] X. Zhang, F. Jia, B. Yang, S. Song, Oxidation of molybdenum disulfide sheet in water under in situ atomic force microscopy observation, J. Phys. Chem. C 121 (2017) 9938–9943, https://doi.org/10.1021/acs.jpcc.7b01863.

[61] P. Rodriguez, F.D. Tichelaar, M.T.M. Koper, A.I. Yanson, Cathodic corrosion as a facile and effective method to prepare clean metal alloy nanoparticles, J. Am. Chem. Soc. 133 (2011) 17626–17629, https://doi.org/10.1021/ja208264e.

[62] T.J.P. Hersbach, A.I. Yanson, M.T.M. Koper, Anisotropic etching of platinum electrodes at the onset of cathodic corrosion, Nat. Commun. 7 (2016) 12653, https://doi.org/10.1038/ncomms12653.

[63] M.L. Kromer, J. Monzó, M.J. Lawrence, A. Kolodziej, Z.T. Gossage, B.H. Simpson, S. Morandi, A. Yanson, J. Rodríguez-López, P. Rodríguez, High-throughput preparation of metal oxide nanocrystals by cathodic corrosion and their use as active photocatalysts, Langmuir 33 (2017) 13295–13302, https://doi.org/10.1021/acs.langmuir.7b02465.

[64] A. Guerfi, L.H. Dao, Electrochromic molybdenum oxide thin films prepared by electrodeposition, J. Electrochem. Soc. 136 (1989) 2435–2436, https://doi.org/10.1149/1.2097408.

[65] A. Guerfi, R.W. Paynter, L.H. Dao, Characterization and stability of electrochromic MoO3 thin films prepared by electrodeposition, J. Electrochem. Soc. 142 (1995) 3457–3464, https://doi.org/10.1149/1.2050004.

[66] M.P. Zach, K.H. Ng, R.M. Penner, Molybdenum nanowires by electrodeposition, Science 290 (2000) 2120–2123, https://doi.org/10.1126/science.290.5499.2120.

[67] Y. Kim, H.W. Kim, S. Lee, J. Han, D. Lee, J.-R. Kim, T.-W. Kim, C.-U. Kim, S.-Y. Jeong, H.-J. Chae, B.-S. Kim, H. Chang, W.B. Kim, S.M. Choi, H.J. Kim, The role of ruthenium on carbon-supported PtRu catalysts for electrocatalytic glycerol oxidation under acidic conditions, ChemCatChem 9 (2017) 1683–1690, https://doi.org/10.1002/cctc.201601325.

[68] D. Lee, Y. Kim, Y. Kwon, J. Lee, T.-W. Kim, Y. Noh, W.B. Kim, M.H. Seo, K. Kim, H. J. Kim, Boosting the electrocatalytic glycerol oxidation performance with highly-dispersed Pt nanoclusters loaded on 3D graphene-like microporous carbon, Appl. Catal., B 245 (2019) 555–568, https://doi.org/10.1016/j.apcatb.2019.01.022.

[69] S.H. Choi, J.S. Lee, XAFS characterization of Pt–Mo bimetallic catalysts for CO hydrogenation, J. Catal. 167 (1997) 364–371, https://doi.org/10.1006/jcat.1997.1578.

[70] A.A. Bessonov, M.N. Kirikova, D.I. Petukhov, M. Allen, T. Ryhänen, M.J.A. Bailey, Layered memristive and memcapacitive switches for printable electronics, Nat. Mater. 14 (2014) 199–204, https://doi.org/10.1038/nmat4135.

[71] X. Long, G. Li, Z. Wang, H. Zhu, T. Zhang, S. Xiao, W. Guo, S. Yang, Metallic iron-nickel sulfide ultrathin nanosheets as a highly active electrocatalyst for hydrogen evolution reaction in acidic media, J. Am. Chem. Soc. 137 (2015) 11900–11903, https://doi.org/10.1021/jacs.5b07228.

[72] T. Prasomsri, T. Nimmanwudipong, Y. Román-Leshkov, Effective hydrodeoxygenation of biomass-derived oxygenates into unsaturated hydrocarbons by MoO3 using low H2 pressures, Energy Environ. Sci. 6 (2013) 1732–1738, https://doi.org/10.1039/C3EE24360E.

[73] M. Dieterle, G. Weinberg, G. Mestl, Raman spectroscopy of molybdenum oxides Part I. Structural characterization of oxygen defects in MoO3–x by DR UV/VIS, Raman spectroscopy and X-ray diffraction, Phys. Chem. Chem. Phys. 4 (2002) 812–821, https://doi.org/10.1039/B107012F.

[74] G. Wang, Y. Ling, Y. Li, Oxygen-deficient metal oxide nanostructures for photoelectrochemical water oxidation and other applications, Nanoscale 4 (2012) 6682–6691, https://doi.org/10.1039/C2NR32222F.